Univerzita Karlova v Praze
Matematicko-fyzikální fakulta

DIPLOMOVÁ PRÁCE

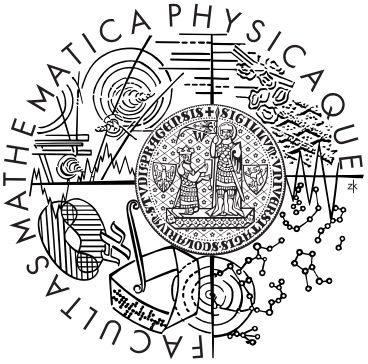

Jiří Svoboda

Radiation of accretion discs around compact objects

Astronomický ústav Akademie věd
Vedoucí diplomové práce: **doc. RNDr. Vladimír Karas**
Studijní program: **Fyzika**
Studijní obor: **Astronomie a astrofyzika**

Chtěl bych poděkovat docentu Vladimíru Karasovi za ochotu a trpělivost při vedení mé diplomové práce.

Prohlašuji, že jsem svou diplomovou práci napsal samostatně a výhradně s použitím citovaných pramenøu. Souhlasím se zapůjčováním práce.

V Praze dne

Jiří Svoboda

Contents

Název práce: *Záření akrečních disků v blízkosti kompaktních objektů*
Autor: *Jiří Svoboda*
Katedra (ústav): *Astronomický ústav Univerzity Karlovy*
Vedoucí diplomové práce: *doc. RNDr. Vladimír Karas, Astronomický ústav Akademie věd, Praha*
E-mail vedoucího: *vladimir.karas@cuni.cz*
Abstrakt: *Tato diplomová práce pojednává o časově rozlišených spektrech záření z vnitřních oblastí akrečního disku okolo černé díry. Zabýváme se v ní studiem profilu původně úzké spektrální čáry rozšířené v důsledku silného gravitačního pole a velmi rychlých rotačních pohybů. Uvažujeme modulaci zářivého toku z důvodu přítomnosti jasné skvrny na disku. Spektrální profily počítáme pro různé hodnoty parametrů a porovnáváme s jednoduššími osově symetrickými případy, které byly již dříve diskutovány různými autory. Naším hlavním cílem je vysledovat v profilu spektrální čáry neaxiální příspěvek jasné skvrny, přičemž bereme v úvahu veškeré relativistické efekty, ovlivňující emitované fotony podél jejich dráhy od disku k pozorovateli. Současná práce představuje první krok v tomto směru.*
Klíčová slova: *akreční disk - profil spektrální čáry - černá díra*

Title: *Radiation of accretion discs around compact objects*
Author: *Jiří Svoboda*
Department: *Astronomical Institute of Charles University*
Supervisor: *doc. RNDr. Vladimír Karas, Astronomical Institute of the Academy of Science, Prague*
Supervisor's e-mail address: *vladimir.karas@cuni.cz*
Abstract: *This diploma thesis deals with the problem of time-dependent spectral features originating from inner regions of black hole accretion discs. We employ the study of a profile of an intrinsic narrow spectral line broadened due to strong gravitational field and very high rotational velocities. We assume modulation of the emitted flux of the disc by an orbiting spot, and we plot the resulting observed flux for different values of the model parameters. We compute the predicted profiles and compare them with similar but simpler situations that have been previously discussed by other authors, such as the radiation signal from an axisymmetric ring or a disc. The main aim of our effort is to trace non-axisymmetric emitting regions (spots) residing on the surface of the disc, taking into account general relativity effects acting on photons along their paths in the gravitational field. The present work gives a first step in this direction.*
Keywords: *accretion disc - line profiles - black holes*

Chapter 1

Introduction

Recent observations from space-based satellites (Chandra, XMM-Newton, etc.) support the idea that supermassive black holes occupy centres of many galaxies. An appropriate way to study black holes is by observing spectra of their accretion discs which are formed by infalling material with nonzero value of angular momentum. The X-ray spectra of active galactic nuclei (AGN) acquired by the satellites suggest the extreme of conditions and very rapid and turbulent motion in such accretion discs. Seyfert galaxies are typical examples of active galaxies, while quasars form rather extreme subclass of AGN. The luminosities of AGN exceed the normal galaxies by four orders of magnitude. This enormous energy output is coming from the region comparable with the size of the solar system. Hence, high luminosities of AGN are explained by an accretion process in a deep potential well of a supermassive black hole. The characteristic values of the mass of the central black hole in AGN are estimated in range $M \approx 10^6 - 10^9 M_\odot$.

In our Galaxy stellar-mass black hole candidates (BHC) exhibit similar spectral features. However, physically these objects are utterly different. They are binary systems in which one component is a black hole and the second one is a star at a later stage of its evolution filling the Roche lobe. Because of much smaller mass these objects are often classified as microquasars. Both types of objects, microquasars and AGN, seem to have similar geometrical structure consisting of a very compact object which is surrounded by an accretion disc and jets. Different is the mass of the central body and characteristic size, $R_g \approx \frac{GM}{c^2} \approx 1.5(\frac{M}{M_\odot})$km. Following this fact the orbital time of spiraling material is much longer for AGN.

We intend to study X-ray spectra which supplement the observations of light curves and surpass the photometry in many aspects. Detailed X-ray spectroscopy reveals the innermost regions. Kα fluorescent line of iron at rest energy at 6.4keV is one of the most notable characteristic features of these spectra. In some cases (such as the Seyfert galaxy MCG 6-30-15) this intrinsically narrow line is observed to be remarkably broadened by Doppler effect and moved in energy by

gravitational redshift which suggests rapid motion and the presence of strong gravity. Hence, the study of the profile of this spectral line is a useful probe of the region very close to a black hole.

We focus our investigation on spectral line profiles taking various approximations of relativistic effects which intend to explain the observed spectral features. The thesis is organized as follows: The brief introduction to the theory of accretion discs and summary of relevant observational facts are described in chapter 2. Chapter 3 serves as a theoretical preliminary to the relativistic models of the spectral line profiles. We introduce the relativistic approximations which are used in the computations of the profiles. These appear in chapter 4. We present theoretical spectral line profiles for radiating rings, spots orbiting at a constant radius and accretion discs. We compare predicted profiles for different values of the geometrical parameters.

By employing a model of orbiting spots we analyze time dependency of the spectral line profiles. We illustrate the time evolution of such a spectral line profile and we aim to trace the spots in the spectrum. We suggest a possible estimation of black hole mass from the parameters of the orbiting spot. In these considerations we assume far better sensitivity of the spectral resolution than present-day instruments allow. The conclusions drawn from our work are summarized in the final chapter 5.

Chapter 2

Accretion discs near compact objects

2.1 Accretion power

Gravitational collapse of normal matter can produce exotic objects such as neutron stars or black holes [28]. Because of their huge value of the mass concentration and tiny volume we call them as compact objects. We can define a compactness parameter as follows [16]:

$$\varepsilon = \frac{2GM}{Rc^2}, \tag{2.1}$$

where R characterises the size of the object. The typical value of the compactness parameter for neutron stars is $\varepsilon \geq 0.1$, while for white dwarfs $\varepsilon \approx 10^{-4}$.

In the following sections we will give a brief introduction to the accretion theory, described in more details in [12]. The mechanism of the accretion power is due to conversion of the gravitational potential energy into radiation. For a body of mass M and radius R we can estimate the energy released by the accretion as:

$$\Delta E_{\mathrm{acc}} = \frac{GMm}{R}. \tag{2.2}$$

From this equation it is clear that the efficiency of the accretion depends on the compactness of the central body defined by eq. (2.1). We can estimate the power of the accretion process from the comparison with the energy output by nuclear fusions. In case of hydrogen burning we obtain:

$$\Delta E \approx 6.10^{18}\mathrm{erg.g}^{-1}. \tag{2.3}$$

For a neutron star with $M \approx M_{\odot}$ and $R \approx 10$km the energy output by accretion on the stellar surface is:

$$\Delta E_{\mathrm{acc}} \approx 10^{20}\mathrm{erg.g}^{-1}, \tag{2.4}$$

which gives even bigger value than the nuclear synthesis.

The maximal luminosity is restricted by the Eddington limit, which is given by:

$$L_{\mathrm{Edd}} = \frac{4\pi G M m_p c}{\sigma_T}, \tag{2.5}$$

where m_p is the mass of a proton (i.e. a nucleus of hydrogen atom) and σ_T is Thomson cross section. The Eddington luminosity represents the highest possible luminosity on the conditions of spherically symmetrical accretion $\dot{M}$ and totally ionized accreting material. In this case, the opacity is dominated by electron scattering[1] and we suffice only with Thomson cross section. For accretion powered objects the Eddington limit implies a limit on the steady accretion rate.

If all the kinetic energy of infalling matter is conversed to radiation at the surface of the central body, then from eq. (2.2) the accretion luminosity L_{acc} is given by:

$$L_{\mathrm{acc}} = \frac{GM\dot{M}}{R}. \tag{2.6}$$

For neutron stars we can re-express eq. (2.6) as:

$$L_{\mathrm{acc}} = 1.3.10^{36}\dot{M}_{16}\frac{M}{M_\odot}\frac{10\mathrm{km}}{R}\mathrm{erg.s}^{-1}, \tag{2.7}$$

where $\dot{M} = 10^{16}\dot{M}_{16}\mathrm{g.s}^{-1}$. For black holes the dimensionless efficiency is needed to be introduced to the relation eq. (2.6). In this case, radius R does not refer to the surface, but it has meaning of the innermost edge of the accretion disc which corresponds to the marginal stable orbit around the black hole. The uncertainty of the value of the luminosity can be parametrized as follows:

$$L_{\mathrm{acc}} = 2\eta\frac{GM\dot{M}}{R} = \eta\dot{M}c^2. \tag{2.8}$$

Thus, the parameter η measures how efficiently the rest mass energy of the accreted material is converted to radiation. Comparing eq. (2.8) with eq. (2.3) we get $\eta = 0.007$ for the burning of hydrogen to helium. The estimation of realistic value for η is an important problem. A reasonable guess would appear to be $\eta \approx 0.1$ [29].

2.2 The emitted spectrum

The radiation temperature is given from thermodynamical considerations:

$$kT_{\mathrm{rad}} \approx h\nu, \tag{2.9}$$

[1] The radiation influences mostly electrons which are of the less mass than protons, vice-versa the gravity more attracts the massive particles. Electrons and protons hold together due to electromagnetic interaction.

where $k \doteq 1.38 \times 10^{-23}\mathrm{J.K}^{-1}$ is Boltzmann constant, $h \doteq 6.626 \times 10^{-34}\mathrm{J.s}$ is Planck constant and ν is the mean frequency. The value of this temperature can be estimated by comparing it with blackbody and thermal temperature:

$$T_{\mathrm{b}} = \left(\frac{L_{\mathrm{acc}}}{4\pi R^2 \sigma} \right)^{\frac{1}{4}}, \tag{2.10}$$

$$T_{\mathrm{th}} = \frac{GMm_p}{3kR}, \tag{2.11}$$

where $\sigma \doteq 5.67.10^{-8}\mathrm{Js}^{-1}\mathrm{m}^{-2}\mathrm{K}^{-4}$ is Stefan-Boltzmann constant. These temperatures are two extremal cases for T_{rad}. If the accretion flow is optically thick, the radiation reaches thermal equilibrium before escaping and $T_{\mathrm{rad}} \approx T_{\mathrm{b}}$. On the other hand, if the conversion to radiation is direct (from optically thin material), then $T_{\mathrm{rad}} \approx T_{\mathrm{th}}$. It gives the limits for the radiation temperature:

$$T_{\mathrm{b}} \leq T_{\mathrm{rad}} \leq T_{\mathrm{th}}. \tag{2.12}$$

For a solar mass neutron star we will give the range for photon energy:

$$1\mathrm{keV} \leq \mathrm{h}\nu \leq 50\mathrm{MeV}. \tag{2.13}$$

Thus, we can expect accreting neutron stars and black holes to appear as X-ray emitters, or possibly γ-ray sources.

2.3 The structure of thin accretion discs

We assumed spherical symmetry in the derivations of the relationships in the section 2.1. However, in any realistic scenario matter with non-zero angular momentum will create an accretion disc around the central object. The previous relations will serve as convenient approximations and estimations. For the description of the disc structure the cylindrical coordinates (R, φ, z) are the most suitable. Next to the axial symmetry, we presume the efficient radiation of the accreting gas. Further, we assume that the angular momentum transport is given by a kinematic viscosity ν. And we suppose that the time scale for redistributing angular momentum is long compared with either the orbital or radiative time scales. Under these assumptions, the gas should form a geometrically thin disc in which fluid elements are orbiting in almost circular paths with angular velocity Ω. Keplerian velocity is a good approximation:

$$\Omega = \sqrt{\frac{GM}{R^3}}. \tag{2.14}$$

The equation for the conservation of mass and angular momentum can be written as:

$$R\frac{\partial \Sigma}{\partial t} + \frac{\partial}{\partial R}(R\Sigma v_R) = 0, \tag{2.15}$$

and

$$R\frac{\partial}{\partial t}(\Sigma R^2 \Omega) + \frac{\partial}{\partial R}(\Sigma v_R R^3 \Omega)) = \frac{1}{2\pi}\frac{\partial G}{\partial R}, \tag{2.16}$$

where

$$G(R,t) = 2\pi R^3 \nu \Sigma \frac{\partial \Omega}{\partial R} \tag{2.17}$$

defines the torque, Σ is the surface density and v_R is the velocity in the radial direction. Combining eqs. 2.15 - 2.17 and using eq. (2.14) we obtain the equation governing time evolution of surface density in the Keplerian disc:

$$\frac{\partial \Sigma}{\partial t} = \frac{3}{R}\frac{\partial}{\partial R}(\sqrt{R}\frac{\partial}{\partial R}(\nu \Sigma \sqrt{R})). \tag{2.18}$$

The kinematic viscosity ν may be a function of local variables in the disc. The eq. (2.18) has the form of non-linear diffusion equation governing the behavior of $\Sigma(R,t)$. Given a solution for $\Sigma(R,t)$ the radial velocity is:

$$v_R = -\frac{3}{\Sigma\sqrt{R}}\frac{\partial}{\partial R}(\nu \Sigma \sqrt{R}). \tag{2.19}$$

We need some prescription for ν to close these equations and permit a full determination of the radial structure of the accretion disc. All of the qualities currently ignored, such as the z-structure or detailed microphysics, enter into the problem via ν.

2.4 The steady thin discs

The equations 2.15 and 2.16 can be rewritten on the condition $\frac{\partial}{\partial t} = 0$ as:

$$R\Sigma v_R = \text{const.} \tag{2.20}$$

and

$$\nu\Sigma = \frac{\dot{M}}{3\pi}\left[1 - \left(\frac{R_{in}}{R}\right)^{\frac{1}{2}}\right], \tag{2.21}$$

where R_{in} means the inner boundary of the disc. In the case of neutron star R is linked with the stellar surface. However, for the material orbiting around a black hole the last stable circular orbit is at the radius $R_{in} = 6R_g$ for Schwarzschild

metric (for Kerr metric of rotating black hole it is closer in dependence on the rate of rotation) [20]. The validity of eq. (2.21) ceases if the central star has a sufficiently strong magnetic field.

The essential idea of the accretion process is dissipation of energy. The dissipation is caused by viscous torques and is given by:

$$D(R) = \frac{G\frac{\partial\Omega}{\partial R}}{4\pi R}. \tag{2.22}$$

Using eq. (2.17) we obtain:

$$D(R) = \frac{1}{2}\nu\Sigma\left(R\frac{\partial\Omega}{\partial R}\right)^2. \tag{2.23}$$

For the Keplerian steady disc we get the relationship for $D(R)$ independent of our ignorance of ν:

$$D(R) = \frac{3GM\dot{M}}{8\pi R^3}\left[1-\left(\frac{R_{in}}{R}\right)^{\frac{1}{2}}\right]. \tag{2.24}$$

The luminosity produced by the disc between radii R_1 and R_2 is given by:

$$L(R_1,R_2) = 2\int_{R_1}^{R_2} D(R)2\pi R dR \tag{2.25}$$

and using eq. (2.23):

$$L(R_1,R_2) = \frac{3GM\dot{M}}{2}\int_{R_1}^{R_2}\left[1-\left(\frac{R_{in}}{R}\right)^{\frac{1}{2}}\right]\frac{dR}{R^2}. \tag{2.26}$$

Setting $R_1 = R_{in}$ and $R_2 \to \infty$, we obtain the luminosity for the whole disc:

$$L_{\text{disc}} = \frac{GM\dot{M}}{2R_{in}} = \frac{1}{2}L_{\text{acc}}. \tag{2.27}$$

If there is a star at the center of the disc, the remaining half of L_{acc} is available to be radiated from the boundary layer. If we suppose that the viscously dissipated energy is radiated as a black body spectrum, using eq. (2.10) we get the relationship for the surface temperature of the disc:

$$T(R) = \left(\frac{3GM\dot{M}}{8\pi\sigma R^3}\left[1-\left(\frac{R_{in}}{R}\right)^{\frac{1}{2}}\right]\right)^{\frac{1}{4}}. \tag{2.28}$$

For a fixed ratio between the source luminosity and Eddington limit and a scaled radius R/M the temperature of the disc depends on the mass as:

$$T(R) \propto M^{-\frac{1}{4}}. \tag{2.29}$$

The thin disc is characterized by no motions or accelerations in the z-direction and the relevant Euler's equation has the form:

$$\frac{1}{\rho}\frac{\partial p}{\partial z} = \frac{\partial}{\partial z}\left[\frac{GM}{(R^2+z^2)^{\frac{1}{2}}}\right], \tag{2.30}$$

where p is the pressure. For a thin disc $(z \ll R)$ we can write:

$$\frac{1}{\rho}\frac{p}{h} = -\frac{GMh}{R^3}, \tag{2.31}$$

where h is the typical vertical scale height of the disc. From eq. (2.31) we can estimate the thickness of the disc as:

$$h \approx \frac{c_s}{\Omega_K} = \frac{c_s R}{v_K}, \tag{2.32}$$

where v_K is the local Keplerian velocity and $c_s = \sqrt{\frac{p}{\rho}}$ is the sound speed.

Now, we can write the criterion for the thin disc as:

$$c_s \ll v_K. \tag{2.33}$$

Thus, the accretion disc is geometrically thin, if the Keplerian velocity is highly supersonic.

2.5 Shakura-Sunyaev model of a steady thin disc

The knowledge of the viscosity ν is required in order to study the detailed physical structure of accretion discs, or any aspect of their time-variability, such as the stability of the accretion disc. A simple and very useful model of the viscosity is α-model or Shakura &Sunyaev model [29]:

$$\nu = \alpha c_s h, \tag{2.34}$$

where α is a dimensionless parameter, which can take the value from 0 to 1. In the first approximation α is a constant for a given accretion disc.

The viscous stress f_φ exerted in the φ-direction can be defined for a Keplerian disc as:

$$f_\varphi = \frac{3}{2}\eta\Omega_K, \tag{2.35}$$

where η is the coefficient of dynamic viscosity. In turbulent motion it can be expressed as:

$$\eta \approx \rho v_{\text{turb}} l_{\text{turb}}, \tag{2.36}$$

where ρ is the matter density, $v_{\text{turb}} \leq c_s$ is the velocity of turbulent cells relative to the mean gas motion and $l_{\text{turb}} \leq h$ is the size of the largest turbulent cells [17, 28]. Using eq. (2.32) we can estimate the value of viscosity stress as:

$$f_\varphi \leq (\rho c_s h)\,\Omega_K \approx \rho {c_s}^2 = P. \tag{2.37}$$

In general, we may write:

$$f_\varphi = \alpha P, \tag{2.38}$$

where α is the same parameter as in eq. (2.34). From eq. (2.19) the radial velocity can be expressed by this model as:

$$v_R \approx \frac{\nu}{R} \approx \frac{\alpha c_s h}{R} \ll c_s. \tag{2.39}$$

Thus, the radial inflow is very subsonic.

Let estimate different time scales: dynamical, thermal and viscous. The dynamical time scale can be defined as:

$$t_{\text{dyn}} = \Omega^{-1}. \tag{2.40}$$

The thermal time scale, on which the dissipated energy is radiated from the accretion disc, is given by:

$$t_{\text{th}} \approx \frac{t_{\text{dyn}}}{\alpha} \tag{2.41}$$

The viscous time scale which is linked with the redistribution of the angular momentum is defined as:

$$t_{\text{visc}} \approx \frac{R^2}{\nu}\left(\frac{R}{h}\right)^2 t_{\text{th}}. \tag{2.42}$$

Comparing the time scales we get this relation:

$$t_{\text{visc}} \gg t_{\text{th}} > t_{\text{dyn}}. \tag{2.43}$$

On dynamical time scales we can well consider the temperature and α parameter independent of time. Although the α-prescription is very successful in many applications, there are some limitations of this approach, especially the presence of the magnetic field. The present-day theoretical models assume that just magneto-rotational instability is responsible for the angular momentum transport. Hence, at least a weak magnetic field is necessary to occur. Its presence in the accreting material leads to the powerful local magneto-hydrodynamical shear instability [2].

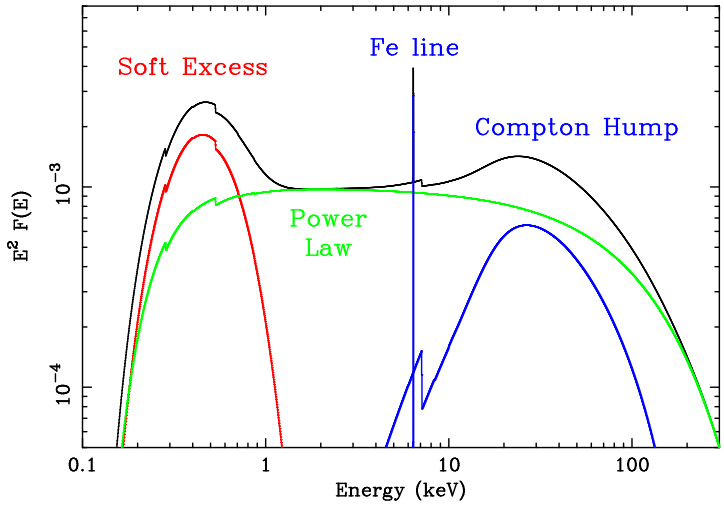

Figure 2.1: Model X-ray spectrum of an AGN [11].

2.6 Accretion disc atmosphere and X-ray reflection

The magnetic field creates flaring events in the places of magnetic reconnections. These processes heat up the hot atmosphere above the accretion disc and generate a hot corona, analogously with the Sun[1]. The presence of the corona is satisfied by many observations of active galactic nuclei or Galactic BHC. The temperature of the disc surface defined by eq. (2.28) is $T \approx 10^5 - 10^6$K for accretion discs around a supermassive black hole making them optical and ultraviolet sources.

However, the characteristic spectrum of AGN (in fig 2.1) has a power-law component extending to hard X-ray energies. The key mechanism of warming up the photons is due to inverse Compton effect. The relatively soft photons coming from the accretion disc surface are shifted in energy by relativistic electrons presented in the hot corona.[2] The geometry of the corona is yet determined ambiguously. The model of the disc surrounding corona ("sandwich" geometry) predicts softer spectra. Such a corona would be cooled by Compton scattering by hot photons from the innermost regions of the disc.

More sophisticated model is a model of a spherical optically thin corona with the typical size of a few R_g ("sphere+disc" geometry). In this geometry the corona is irradiated only by soft photons from the cool outer parts of the disc [9, 32]. A model of such a X-ray reflected spectrum is presented in fig 2.1, [11]. There are four prominent features of the spectrum. The underlying power-law component

[1]This idea was first mentioned in [13] and requires presence of at least a week magnetic field and differential rotation of the accretion disc

[2]Alternative models suppose hot inner flows which are formed when the inner edge of accretion disc does not refer to the last stable orbit around a black hole.

was already discussed. The soft excess corresponds with a change of the continuum slope. The nature of this bump is not well understood. It can be due to the thermal Comptonization or emission by bremsstrahlung. Approximately 50% of all Seyfert galaxies have characteristic absorption lines in the soft excess of their spectra. They are created by photo-absorption in a highly ionized medium, the so-called warm absorber. An emission line around 6.4keV[3] and a hardening of the power-law continuum above 10keV are the imprints of the reflected spectrum [14, 24, 26]. It is produced by Compton scattering, fluorescence of iron atoms and any other emission from the disc associated with the hard X-ray illumination.

[3]The conversion between energies and frequencies is given by the Planck's equation $E = h\nu$, $\nu\,[\mathrm{Hz}] \doteq 0.24 \times 10^{18} E\,[\mathrm{keV}]$.

Chapter 3

Emission lines of accretion discs

3.1 Fe Kα line

As was discussed in the previous chapter many AGN have a prominent emission line around 6.4keV (such as in fig 3.1), which corresponds to the Kα line of neutral iron atom.[1] The Fe Kα line is thought to be a fluorescent line which originates from inner parts of the accretion disc due to the irradiation of some X-ray source which is above the accretion disc (e.g. from the corona) [10, 21]. There are other possible explanations of its presence, such as the process of Comptonization on some cold clouds which occur in the corona. We follow the idea of the origin from the inner parts of the accretion disc, which can be well-satisfied by an enormous broadening of this line. This could be explained by high velocities of accreting matter in the close vicinity of a supermassive black hole. The effects of the fast rotation and the strong gravity will be analysed in this chapter and employed in the calculations in the next chapter.

Not only that the iron line is present in the X-ray spectrum, but it is often the most outstanding one. The strength of the emission line is convenient to adjudicate via the use of equivalent widths. The equivalent width of an emission line is defined as the energy (or wavelength) range over which the continuum radiation contains a flux equal to that contained in the emission line. For Fe Kα line the equivalent width of the observed profile can reach approximately 180eV. The other emission lines are much weaker, with equivalent widths at least an order of magnitude less.

The presence of the Fe Kα line is affected by physical conditions of the disc atmosphere, especially due to the ionization rate of the matter. The ionization

[1] In fact, the Kα emission line is a doublet comprising of the Kα1 at 6.404keV and Kα2 at 6.391keV.

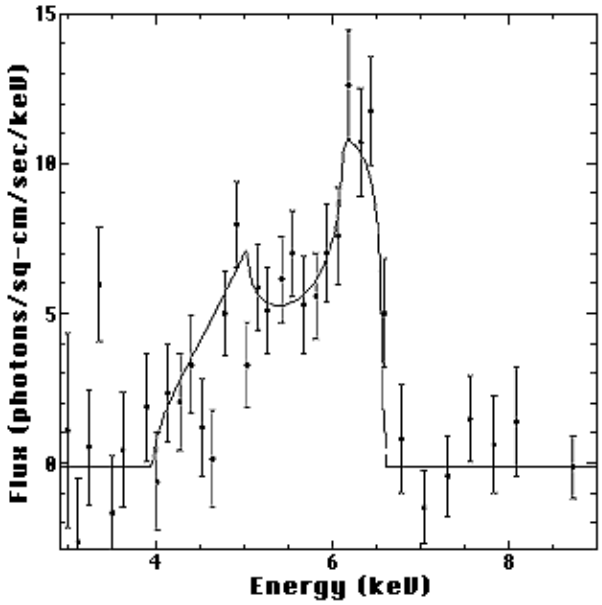

Figure 3.1: Fe Kα emission line at spectrum of MCG 6-30-15 (Tanaka et al., 1995).

parameter is defined as:

$$\xi(R) = \frac{4\pi F_x(R)}{n(R)}, \tag{3.1}$$

where F_x is the flux received per unit area of the disc at a radius R, and $n(R)$ is the comoving electron number density. For fully-ionized regime ($\xi > 5000$erg.cm.s^{-1}) the Fe Kα line is missing.

3.2 Broadening of a spectral line by Doppler effect

If the Fe Kα originated from the accretion disc the rapid rotation influences the spectral line profile by Doppler effect. From the receding parts of the disc the observed spectral line is shifted to the lower frequencies (to the red) and contrary from the approaching parts it is shifted to the higher frequencies (to the blue). It consequently leads to the double-horned profile, e.g. [18]. If the rotational velocities are non-relativistic and the attendant gravitational field is weak, the frequency of the observed spectral line ν_{obs} is given by classical Doppler relationship:

$$\frac{\Delta\nu}{\nu_{\rm em}} = \frac{\nu_{\rm obs} - \nu_{\rm em}}{\nu_{\rm em}} = -\frac{RV}{c}, \tag{3.2}$$

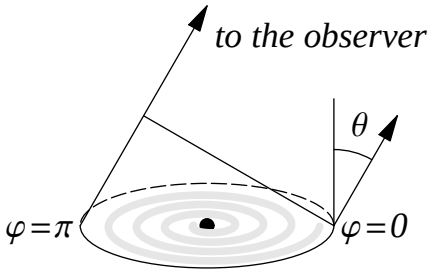

Figure 3.2: The angle convention.

where ν_{em} is the emitted frequency and RV is the radial velocity from the observer (line-of-sight velocity). RV is positive if the matter is receding and negative if the matter is approaching. For orbits with circular velocities v_φ it is given by:

$$RV = v_\varphi \cos\varphi \sin\theta, \tag{3.3}$$

where φ is the azimuthal angle and Θ is the angle of the inclination. The used convention is such that φ is equal to zero at the nearest point to the observer and goes with the direction of the disc rotation. The inclination angle Θ is equal to zero for the "face-on disc" (when observer's line of sight is perpendicular to the plane of the disc). From eq. (3.2) and eq. (3.3) it is evident that no frequency shift would be observed in this case of the inclination angle. $\Theta = \frac{\pi}{2}$ corresponds to the disc being in the same plane as the line of sight ("edge on disc"). Described angle convention is illustrated in fig 3.2.

Using eq. (2.14) we can rewrite eq. (3.3) as:

$$RV = \sqrt{\frac{GM}{R}} \cos\varphi \sin\theta, \tag{3.4}$$

From this relation it is clear that the most shifted frequencies, which form the spectral line wings, are linked with radiation coming from the innermost parts of the disc at $\varphi \approx \frac{\pi}{2}$ for the red shifts (resp. $\varphi \approx \frac{3\pi}{2}$ for the blue ones).

If the orbital velocities v_φ do not fulfill the condition $v_\varphi \ll c$, the special relativistic transverse Doppler effect has to be taken into account. In special relativity propagation 4-vector k^μ is defined as:

$$k^\mu = \left(\frac{\omega}{c}, \mathbf{k}\right), \tag{3.5}$$

where $\omega = 2\pi\nu$. In the moving frame:

$$k'^\mu = \Lambda^\mu{}_\rho k^\rho, \tag{3.6}$$

where $\Lambda^{\mu}{}_{\rho}$ is the Lorentz matrix and ρ is the summing index. If we set x-axis as the line of sight:

$$k'^{0} = \frac{\omega'}{c} = \Lambda^{0}{}_{0}k^{0} + \Lambda^{0}{}_{1}k^{1} = \gamma\frac{\omega}{c} - \frac{RV}{c}\gamma\frac{\omega}{c}, \tag{3.7}$$

where

$$\gamma = \frac{1}{\sqrt{1-\frac{v^2}{c^2}}}.$$

Thus,

$$\nu_{\mathrm{obs}} = \frac{1}{\gamma\left(1-\frac{RV}{c}\right)}\nu_{\mathrm{em}}. \tag{3.8}$$

From eq. (3.8) the frequency of the spectral line is even shifted for the case of the face-on disc when $RV = 0$. Then the observed frequency is given by the value of the emitted frequency multiplied by inverse γ-factor which is always less than unity. So, the spectral line is shifted to the red. This effect is called as the transverse Doppler shift. The value of the shift depends on the value of orbital velocity.

3.3 An asymmetry between two peaks

Liouville's theorem belongs among key theorems of Hamiltonian mechanics. It declares that the phase-space volume Γ is invariant to the canonical transformations, which represent time evolution of the system.

$$\int_{\Gamma} \mathrm{d}^{n}p\mathrm{d}^{n}q = C, \tag{3.9}$$

where n is dimension, q expresses coordinates and p the conjugated momenta. In our application the Liouville's theorem states that the phase-space density:

$$n = \frac{N}{\Gamma}, \tag{3.10}$$

is a constant of the Lorentz transformation. N is the number of photons. The element of the phase-space volume is given by:

$$\Gamma = \mathrm{d}^{3}p\mathrm{d}^{3}x = 4\pi p^{2}\mathrm{d}p\mathrm{d}\Omega cS\mathrm{d}t. \tag{3.11}$$

Thus,

$$n = \frac{N}{4\pi p^{2}\mathrm{dpd}\Omega\mathrm{cSdt}}. \tag{3.12}$$

The intensity I is defined as energy emitted at some given frequency into the element of solid angle in an unit of time:

$$I = \frac{Nh\nu}{\mathrm{d}t\mathrm{d}\nu\mathrm{d}\Omega}. \tag{3.13}$$

Substituting from eq. (3.10) into eq. (3.13) and using $p = \frac{h\nu}{c}$:

$$I = \frac{4\pi h^4 cSn\nu^3}{c^3}, \tag{3.14}$$

and

$$\frac{I}{\nu^3} = const. \tag{3.15}$$

Let introduce a *g-factor* for the calculation of the value of the observed frequency from the emitted one:

$$\nu_{\mathrm{obs}} = g\nu_{\mathrm{em}}, \tag{3.16}$$

where $g = g(R, \varphi, \theta)$. From the previous relations we get:

$$g_{\mathrm{class}} = 1 - \frac{RV}{c}, \tag{3.17}$$

and

$$g_{\mathrm{STR}} = \frac{1}{\gamma\left(1 - \frac{RV}{c}\right)}. \tag{3.18}$$

From eq. (3.15) follows:

$$\frac{I_{\mathrm{obs}}}{I_{\mathrm{em}}} = \frac{{\nu_{\mathrm{obs}}}^3}{{\nu_{\mathrm{em}}}^3} = g^3. \tag{3.19}$$

This fact implies the asymmetry between two peaks of the spectral line and makes the blue horn higher than the red one.

3.4 The effects of general relativity

Nor special relativity explains all observed features of the spectral line profile, but general relativity probably does. The effects of general relativity are remarkable if the mass concentration of the central body achieves values comparable with neutron stars or black holes and the accreting material is orbiting within a few hundreds of gravitational radii:

$$R \leq 10^2 R_g, \tag{3.20}$$

where

$$R_g \equiv \frac{GM}{c^2}. \tag{3.21}$$

This is a case of both objects of our interest. Hence, we find gravitational effects responsible for the spectral line features rather than any microphysics.

For non-rotating or very slow rotating central bodies with no electric charge the space-time is described by Schwarzschild metric:

$$ds^2 = -\left(1-\frac{2}{R}\right)dt^2 + \frac{1}{\left(1-\frac{2}{R}\right)}dR^2 + R^2 d\Omega^2, \tag{3.22}$$

where geometrized units $(c = G = 1)$ are used, radius R is measured in units of mass of the central body and $d\Omega^2 \equiv d\theta^2 + \sin^2\theta d\varphi^2$. These scaled quantities are convenient also for further calculations and are used if it is not explicitly written else. The motion of the test particle is due to the geodesic equation:

$$\frac{du^\mu}{d\tau} + \Gamma^\mu{}_{\nu\sigma} u^\nu u^\sigma, \tag{3.23}$$

where τ is the proper time, u^μ four-velocity and $\Gamma^\mu{}_{\nu\sigma}$ the connection coefficients defined by the metric tensor and its first derivations.

The redshift factor $g = g(R,\varphi,\theta)$ defined by eq. (3.16) can be expressed within the approximation of geometrical optics, in terms of four-momentum of photons p_μ and four-velocities u^μ:

$$g = \frac{\left(p_\mu u^\mu\right)_{\rm obs}}{\left(p_\mu u^\mu\right)_{\rm em}}. \tag{3.24}$$

Using $u^\mu{}_{\rm obs} = [-1,0,0,0]$ (four-velocity of the observer):

$$g = \frac{-\left(p_t\right)_{\rm obs}}{\left(p_\mu u^\mu\right)_{\rm em}}. \tag{3.25}$$

The computation of g-factor can be provided numerically [8], or it is feasible to make some approximations. The eq. (3.25) can be modified in the following way:

$$g = \frac{1}{u_e{}^t\left[1-\Omega_{\rm Kep} l(r,\varphi,\theta)\right]}, \tag{3.26}$$

where $u_e{}^t = \left(1-\frac{3}{r}\right)^{-\frac{1}{2}}$ is a component of the disc Keplerian four-velocity and $l(r,\varphi,\theta)$ is the azimuthal component of the photon's angular momentum. The dependence of $l(r,\varphi,\theta)$ on the polar coordinates can be calculated via using of elliptical functions [4].

The another analytical approximation of g-factor has employed Pecháček et al. [22]:

$$g = \frac{\sqrt{R(R-3)}}{R + \sqrt{R-2+4(1+\cos\varphi\sin\theta_0)^{-1}}\sin\varphi\sin\theta_0}, \tag{3.27}$$

which includes light bending according to Beloborodov's approximating formula [3]. Details of the calculation are described in [8, 22] and in publications cited therein.

The very important task is to inspect the maxima of this function in dependence on the azimuthal angle φ. In the Newtonian and also in the special relativistic approach the maxima of g occur at $\varphi = \frac{\pi}{2}$ for the redshift, respective at $\varphi = \frac{3}{2}\pi$ for the blueshift. However, in the general relativity approximation, in which the light bending is included, the maxima move out from their Newtonian values.

The values of the azimuthal angles joined with the maximal shifts are given by an extremal condition:

$$\frac{\partial g}{\partial \varphi} = 0. \tag{3.28}$$

$$g_{\pm} = \frac{\sqrt{R(R-3)}}{r + \sqrt{r-2+4\left(1+\cos\varphi_{\pm}\sin\theta_{\mathrm{o}}\right)^{-1}}\sin\varphi_{\pm}\sin\theta_{\mathrm{o}}}. \tag{3.29}$$

These extremal values occur for the azimuthal polar coordinate $\varphi \equiv \varphi_{\pm}$, defined by:

$$\sin\varphi_{\pm} = \mp\left(1-\cos^2\varphi_{\pm}\right)^{1/2}, \tag{3.30}$$

$$\cos\varphi_{\pm} = f_1{}^{-1}\left[f_2{}^{1/3} + (r-4)^2 f_2{}^{-1/3} - 2(r-1)\right]. \tag{3.31}$$

The functions $f_1(r,\theta_{\mathrm{o}})$ and $f_2(r,\theta_{\mathrm{o}})$ are

$$f_1(r,\theta_{\mathrm{o}}) = 3(r-2)\sin\theta_{\mathrm{o}}, \tag{3.32}$$

$$f_2(r,\theta_{\mathrm{o}}) = (r-4)^3 + f_3{}^2 + \left[2(r-4)^3 + f_3{}^2\right]^{1/2} f_3, \tag{3.33}$$

with $f_3(r,\theta_{\mathrm{o}})$ being

$$f_3(r,\theta_{\mathrm{o}}) = 3\sqrt{3}\,(r-2)\cos\theta_{\mathrm{o}}. \tag{3.34}$$

Chapter 4

Predicted profiles of the emission line

4.1 Assumptions of the models

The motivation for our work is to explain the observed spectral line profiles, such as in fig 3.1. We believe to attain more understanding of the observational facts by modeling of the spectral line profiles for different parameters, such as the inclination of the disc, its size or flux distribution on the disc. A lot of theoretical studies and numerical computations were done in last three decades, such as in [1, 8, 10, 15, 21, 25] and cited therein, but many aspects stay still unclear.

In this chapter we present the computed spectral line profiles of radiating rings at first. We show the differences between Newtonian and relativistic approaches. Then we present spectral line profiles of accretion discs. We show an example of the profile for an accretion disc with an addition coming from a hot spot. On this example we illustrate the procedure of determination of the radius of the spot from the centre. Satisfied by better spectral resolution of the observational instruments in near future (pledged by the scientist's team preparing the Constellation-X mission, *www.nasa.gov*) we intend to study time dependent spectra. By analysing of time variations of the profile, caused by a presence of a spot on the disc, we could be even rightful to estimate a black hole mass. We have an analogical situation to binaries research but complicated by possibly much more spots on the disc and especially not persistent occurrence of the spots. The main aim of our effort is to trace the spots residing on the surface of the disc, taking into account general relativity effects acting on photons along their paths in the gravitational field.

For our numerical calculations we made some simplifying assumptions. In particular, we consider geometrically thin disc which is optically thick. Thus, we assume the validity of the condition presented in eq. (2.33), which is well enti-

tled for fast rotating relativistic discs. In consistence of the previous assumption and eq. (2.42) we suppose that the radial inflow is neglectable compared with the orbital velocity. Thus, we consider only azimuthal motion of the accreting material which is given by the Keplerian velocity, eq. (2.14). We do not mention any external non-gravitational force at all, even a presence of magnetic field. Further, we assume radiation from the disc to be isotropic. We consider non-rotating or relatively slowly rotating central body and Schwarzschild's metric appropriate to this fact. The spectral line profile can be modified by computations for fast rotating black holes in Kerr's metric [5, 7, 25]. The characteristic relativistic features are preserved for both types of space-time. In Kerr's metric an extra parameter a, which describes the rotation of the black hole, incomes into the account. In the following models of the spectral line profiles we suffice with Schwarzschild's metric and the approximation of the frequency shift defined by eq. (3.27).

4.2 Spectral line profiles of rotating radiating rings

Before we will discuss about the spectral line profiles of the whole accretion discs, we show profiles respective to the rotating radiating rings. Then, the accretion disc can be modeled as a composition of such narrow rings. Moreover, one can see on the spectrum of a radiating ring as some mean profile on which a contribution from a circulating bright spot may be occasionally superposed. We also purpose to illustrate the difference between Newtonian and relativistic approach in this part.

Thus at first, we present a spectral line profile for a radiating ring influenced only by rotation, computed by using the classical relationship for Doppler shift of the frequency given by eq. (3.2). The resulting profile for a radiating ring at $R = 6R_g$ is illustrated in fig 4.1. There are three curves in the graph for different values of the inclination angle. The quantity flux represents relative number of photons in the relevant interval of frequencies. The sum of all contributions from the energy channels is normalized to the one (the details of the calculations are described in app. A). The frequency shift on the x-axis is expressed in terms of the radial velocity, according to the eq. (3.2). The profile has two prominent peaks on the wings of the spectral line which are symmetrically shifted to the red (lower values of energy) when the rotating material is receding, and to the blue (higher values of energy) when it is approaching. By comparing of the three curves it is obvious that the bigger frequency shifts occur for bigger angles of the inclination.

The symmetry of the profile is broken down when we apply the special relativistic approach, see fig 4.2. The blue horn is remarkably higher than the red one, which is due to the Liouville's theorem, eq. (3.15). This concentration of the intensity in the direction of the motion is called as relativistic aberration.

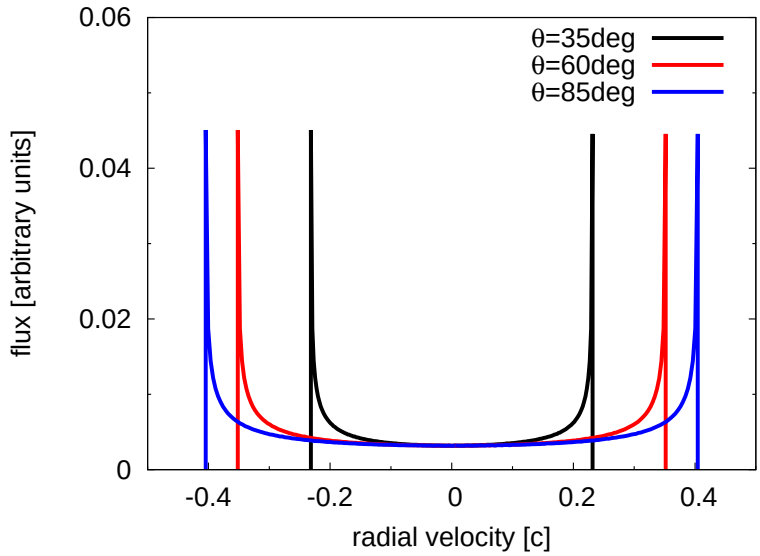

Figure 4.1: The spectral line profile for a radiating ring at $R = 6R_g$ in the Newtonian approach.

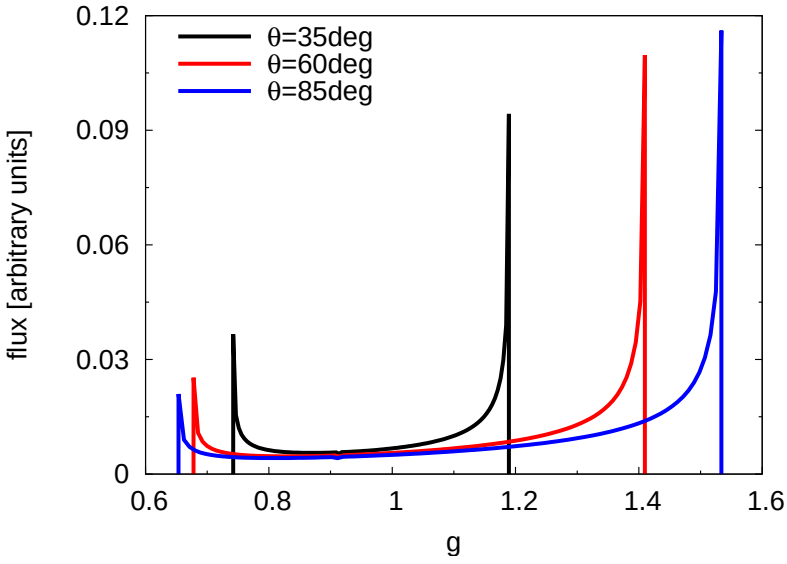

Figure 4.2: The spectral line profile for a radiating ring at $R = 6R_g$ in the special relativistic approach.

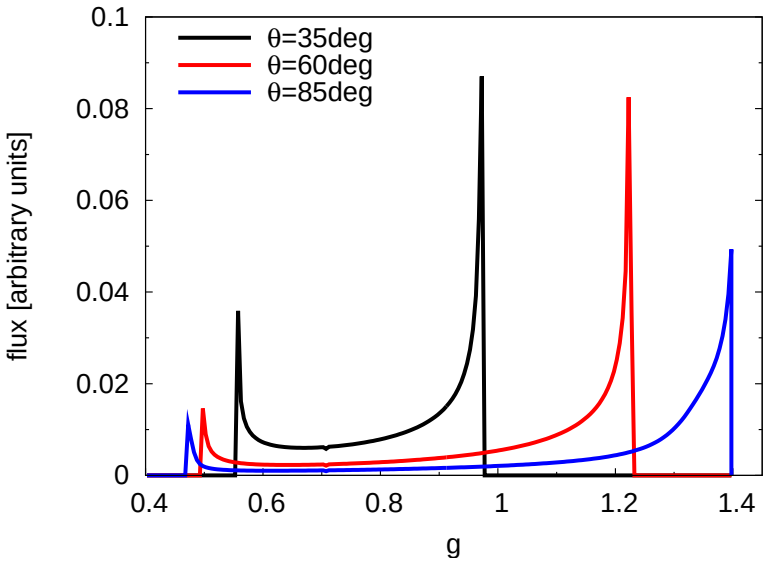

Figure 4.3: The spectral line profile for a radiating ring at $R = 6R_g$ in the general relativistic approach.

The gravitational redshift is significant in general relativity. The spectral line is shifted to the lower frequencies in dependence on the distance from the gravitational centre. The resulting profile for a radiating ring at $R = 6R_g$ is illustrated in fig 4.3. Comparing with the two previous figures this one best matches the observation of MCG 6-30-15 in fig 3.1.

The figures 4.4 - 4.6 represent numerical calculations of such profiles for different values of the radius and the inclination angle. The intrinsic frequency is expressed by a dotted line in the graphs.

It is obvious that the relativistic effects, such as gravitational redshift or aberration, are outstanding for rings which are closer to the black hole. Supposing the Keplerian orbital velocity the rotational velocity decreases with the radius and hence Doppler broadening is also more emphasized by the innermost rings. The dependence of the Doppler broadening on the inclination angle was yet discussed and it is clear that the line is the more shifted the more inclined orbit we consider.

The gravitational redshift entails that some spectral lines are whole found at lower frequencies than the intrinsic one, with the inclusion of their broadened wings. This occurs when the inclination angle is not high enough to overstrike the gravity by the Doppler shift. The total broadening of the line of any inclined ring always decreases with the increasing distance from the centre. However, the maximal blueshift strongly depends on the value of the inclination angle θ. This fact is clearly seen on a comparison of profiles of different inclinations. While for

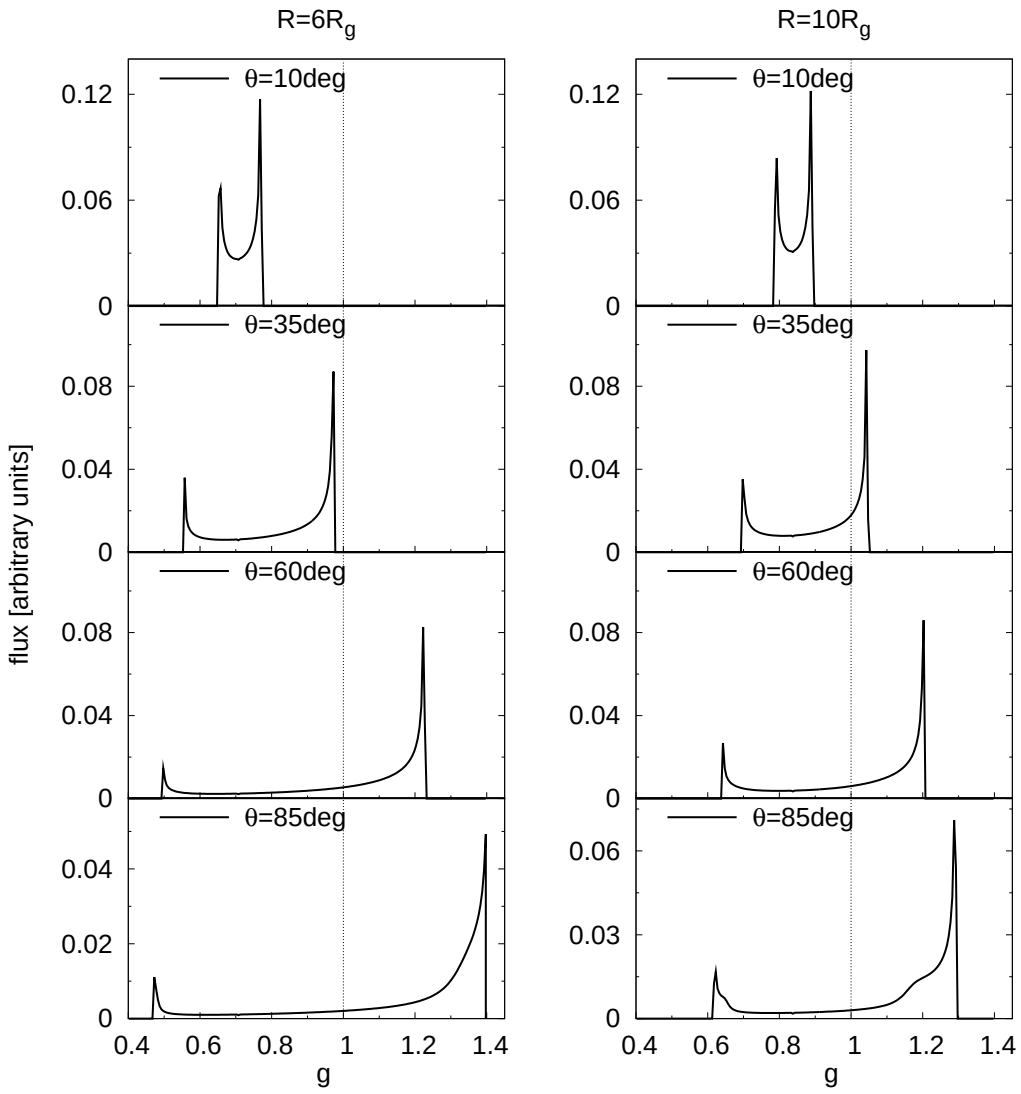

Figure 4.4: The spectral line profile for a radiating ring at $R = 6R_g$ (left panel) and $R = 10R_g$ (right panel) for different values of the inclination angle.

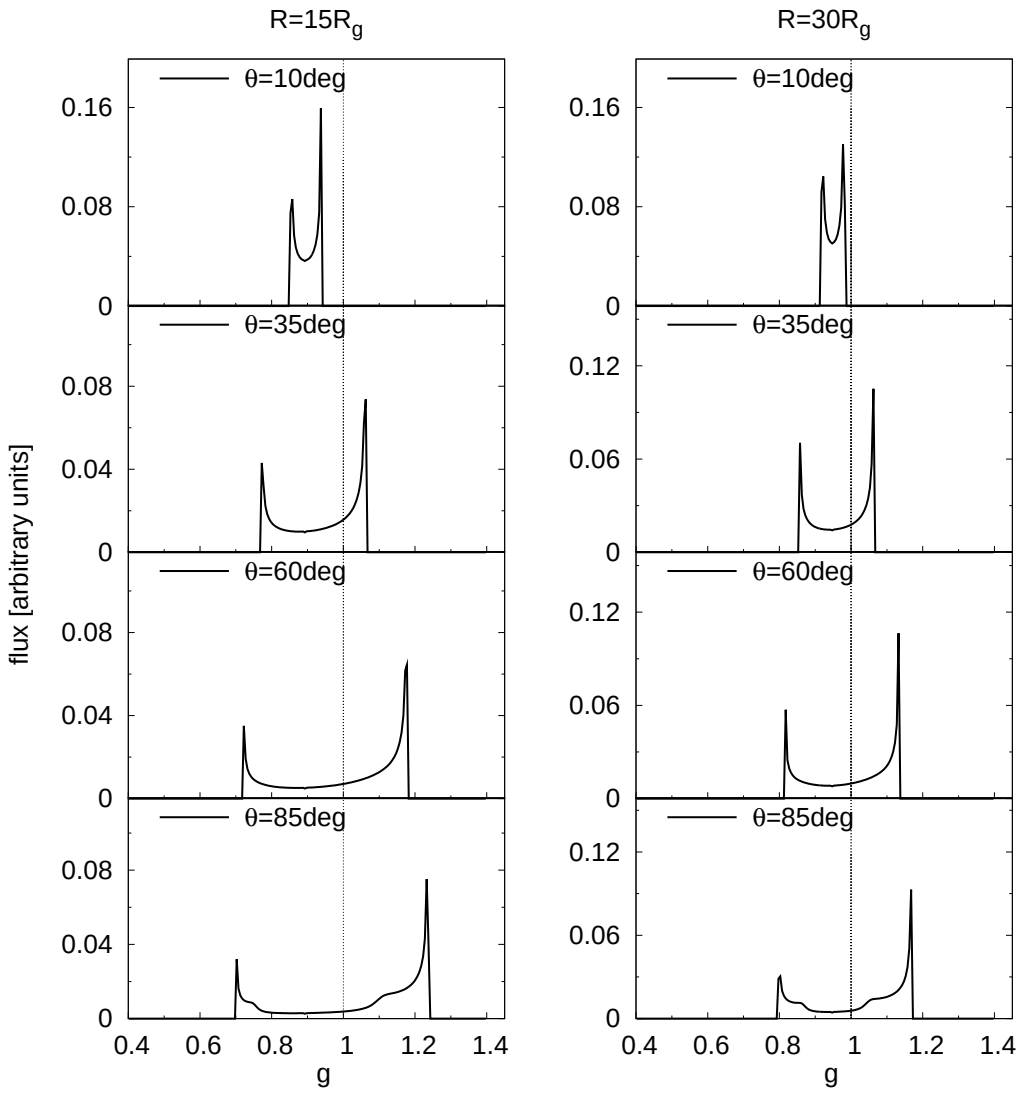

Figure 4.5: The spectral line profile for a radiating ring at $R = 15R_g$ (left panel) and $R = 30R_g$ (right panel) for different values of the inclination angle.

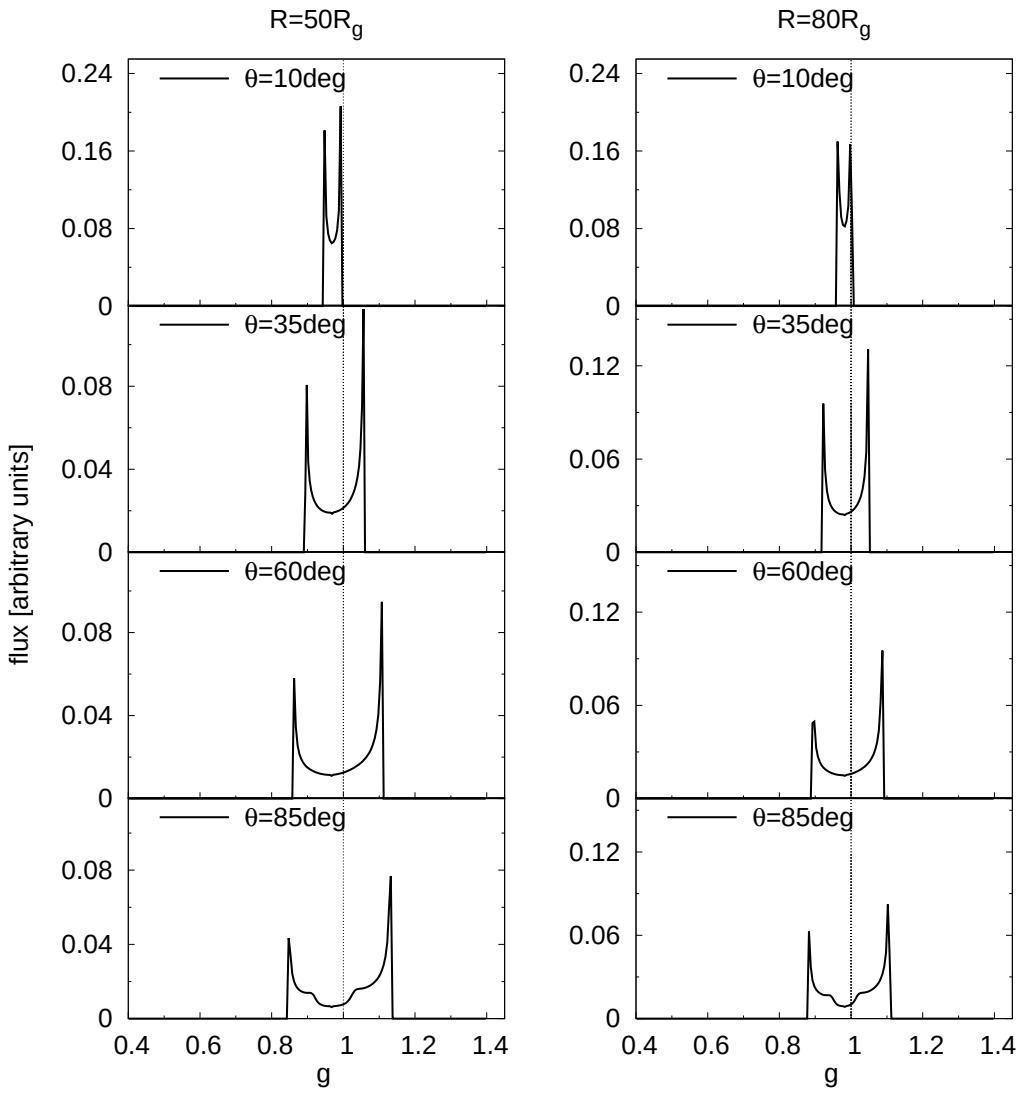

Figure 4.6: The spectral line profile for a radiating ring at $R = 50R_g$ (left panel) and $R = 80R_g$ (right panel) for different values of the inclination angle.

$\theta = 85$deg Doppler broadening is much more remarkable than the gravitational redshift, for $\theta = 35$deg the more blueshift appears at $R = 30R_g$ than at the innermost orbit $R = 6R_g$. The spectral line with $R = 6R_g$ and $\theta = 35$deg belongs to the examples of totally redshifted lines.

4.3 Spectral line profiles of accretion discs

As was mentioned at the beginning of the previous section, an accretion disc radiates as a lot of narrow rotating rings. In computations we set a certain values of the integrational steps dR, dφ. The disc is then divided disc into the amount of infinitesimal radiating areas, which are naturally of different size. The surface of generated radiating elements depends on the radius and it is given by:

$$S = \pi \left[(R + \mathrm{d}R)^2 - R^2 \right] \frac{\mathrm{d}\varphi}{2\pi} \approx R\mathrm{d}R\mathrm{d}\varphi, \tag{4.1}$$

where dR and dφ are the integrational steps. The total profile of a spectral line emitted from the disc is influenced by geometry of the disc. We consider only thin axially symmetric discs. The inner and the outer edge stay free parameters. In our calculations we take $R = 6R_g$ as a lower limit which is a natural choice regarding the last stable circular orbit in Schwarzschild metric.

The radiation flux distribution over the disc is another important parameter of the model. We assume a simple dependence upon the radius and that the intrinsic spectral line is a δ-function in energy:

$$I(R,E) = I_0 \delta(E - E_0) R^{-q}, \tag{4.2}$$

where q is a dimensionless parameter. For Shakura-Sunyaev discs $q \approx 2$. In [10] the authors expect that $q \approx 0$ for radii below some critical value $R < R_c$, $q \approx 2$ where $R \approx$ a few R_c and $q \approx 3$ beyond. The critical value R_c corresponds to the outer radius of the corona. The assumption of the intrinsic spectral line as a δ-function in energy is satisfied by analysing specifically narrow spectral lines, such as the Fe Kα line.

The spectral line profiles of accretion discs with various values of the parameters are illustrated in fig 4.7. The profiles are different from the profiles of rings, especially in positions of the peaks. By discs, the hornes do not occur in the wings of the line. It is a direct consequence of the geometrical properties of the disc and the presumed decrease of the orbital velocity with the increasing distance. The outer parts are not allowed to reach such values of the line-of-sight velocities as the inner parts of the disc. Thus, the wings of the line are formed only by radiation coming from the innermost parts of the disc at $\varphi \approx \frac{\pi}{2}$ (resp. $\varphi \approx \frac{3\pi}{2}$). This fact is

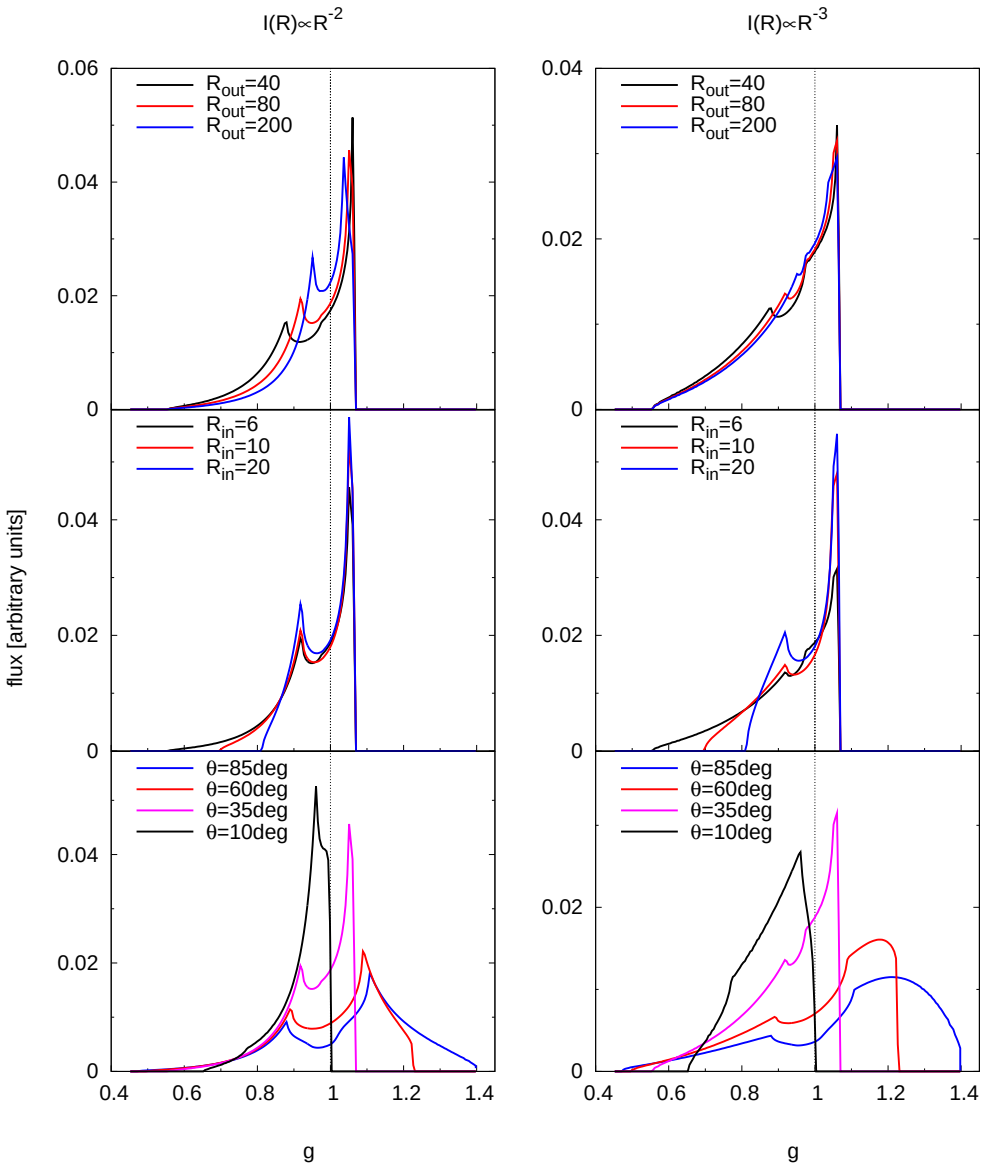

Figure 4.7: The spectral line profile for accretion discs with $I(R) \approx R^{-2}$ (left panel) and $I(R) \approx R^{-3}$ (right panel) for different values of the parameters. When not specified in labels, the other parameters are fixed at $R_{\rm in} = 6R_g$, $R_{\rm out} = 80R_g$ and $\theta = 35$deg.

also seen on the comparison between two dependencies of the radiation flux distribution upon the radius R. At the left panel of fig 4.7 the spectral line profiles are calculated for $q = 2$, while at the right panel of the figure for $q = 3$. Apparently, the wings are stronger for the steeper decrease of radiation flux.

Figure (4.7) illustrates also the dependency of the spectral line profile on the other parameters of the disc. The most appreciably, the profile depends on the inclination angle θ, as is showed in the bottom graphs. The more shifted lines belong to the discs with higher inclination angles. The value of the inner edge of the disc R_{in} influences the shape of the wings. The positions of the peaks are sensitive to the value of the outer edge of the disc (middle graphs). The peaks of the more extended discs occur closer to the intrinsic frequency due to the decrease of the orbital velocity with the radius R. It is clear that for the steeper decrease of radiation flux the outer parts have less influence. Hence, the differences for variable values of R_{out} are more apparent for a lower value of q (at the left panel), while the dependence on R_{in} is more appreciable for higher values of q (at the right panel).

4.4 Hot spot on the disc

In the previous section we assumed an isotropic distribution of the radiation flux. However, one can expect the formation of some inhomogeneities, hot spots, which would orbit at an extensional radius and their occurrence would last at least a time comparable with the orbital time of the spot. If the brightness of such a spot were high enough, then the corresponding peaks would appear in the spectral line profiles, as in fig 4.8. After insetting a profile of an accretion disc with the most suitable parameters the peaks belonging to the spot are clearly seen, especially the red one (fig 4.9). We find the profile of an accretion disc with the inclination $\theta = 35$deg and $R_{\rm outer} \approx 40R_g$ as optimal.

Considering time averaged spectra the spectral line profile of the contingent spot has the same character as the profile of a radiating ring, section (4.2). So, the horns linked with the spot occur at the most shifted energies relative to the radius from the centre. Thus, from the positions of that horns at spectra we can estimate a value of the radius from the centre R of the spot. For this purpose we look for a relation between extremal frequency shift $g_{\pm}$ and the radius R.

In the Newtonian or special relativistic approach the azimuthal polar coordinates $\varphi_- = \frac{1}{2}\pi$ (resp. $\varphi_+ = \frac{3}{2}\pi$) correspond to the extremal redshift (resp. blueshift), but not so in general relativity, where we have a set of rather complicated equations (3.29)-(3.34). However, for a casual estimation of the radius R of the spot from fig 4.9 we can make an approximation that the values of the extremal azimuthal coordinates do not differ from their Newtonian values.

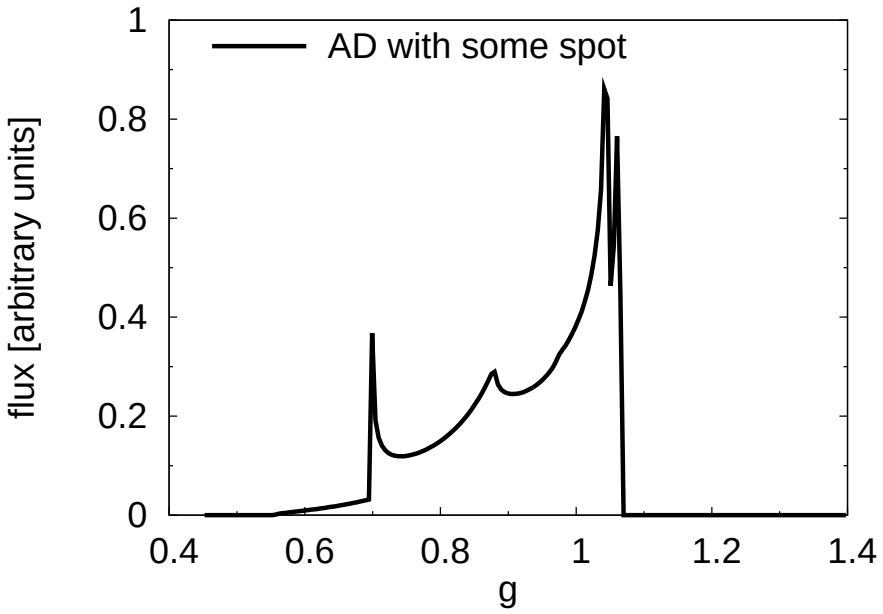

Figure 4.8: An example of a spectral line profile of an AD with a hot spot on its surface.

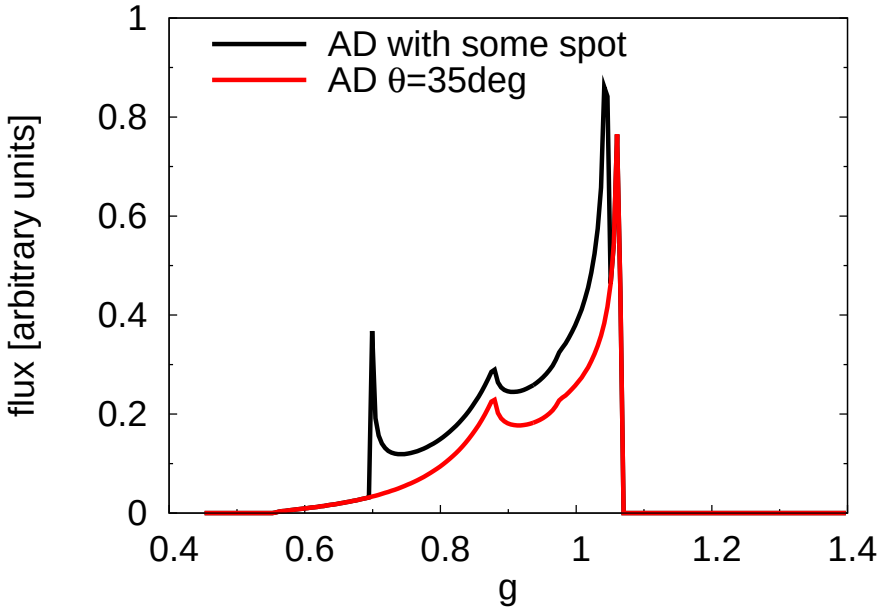

Figure 4.9: An identification of a hot spot in the spectral line profile.

We begin our analysis by the red horn which is more transparent than the blue one. The frequency shift g at $\varphi = \frac{\pi}{2}$ has the form:

$$g = \frac{\sqrt{R(R-3)}}{R + \sqrt{R+2}\sin\theta}. \tag{4.3}$$

We get:

$$0 = (g^2-1)R^2 + (g^2\sin\theta_0 + 3)R + 2g^2R\sqrt{R+2}\sin\theta_0 + 2g^2\sin\theta_0. \tag{4.4}$$

Dividing this equation by R and neglecting of the last component:

$$\frac{2g^2\sin\theta_0}{R} \to 0, \tag{4.5}$$

we obtain a quadratic equation:

$$\begin{aligned} 0 =& \left(g^2-1\right)^2 R^2 + \left[2\left(g^2-1\right)\left(g^2\sin\theta_0+3\right) - 4g^4\sin^2\theta\right] R \\ &+ \left[\left(g^2\sin\theta_0+3\right)^2 - 8g^4\sin^2\theta\right]. \end{aligned} \tag{4.6}$$

For $g = 0.7$ and $\sin\theta_0 = \sin(35\text{deg}) \doteq 0.57$ we get:

$$R_{1,2} \simeq \begin{cases} 10.3 \\ 3.8 \quad (< 6!) \end{cases}. \tag{4.7}$$

One root of the quadratic equation has the value under $6R_g$, which suggests that the other is right. Otherwise, we have to solve analogical equation for the blueshift.[1]

The values of g and θ are determined with some measurement errors. Supposing $\Delta g \approx 0.02$ and $\Delta\theta \approx 5\text{deg}$ the limits for the radius R are:

$$8.8R_g \leq R \leq 12.1R_g, \tag{4.8}$$

which gives a good estimation of the distance of the spot. In fact, fig 4.8 represents a composite spectral line from the accretion disc and the radiating ring (time-averaged profile of the spot) at $R = 10R_g$ with the inclination angle $\theta = 35\text{deg}$. The rough estimation seems to be rightful within the measurement errors.

This method can be particularly applied for more distant radii and lower inclination angles, when the relativistic effects are not too strong and the azimuthal

[1] The blueshift of the spectral line from the inner orbits is significantly overstriked by gravitational redshift. While the red wing is shifted the more the closer the orbit to the black hole is, the most shifted blue wings occur for spots at more distant radius ($\approx 15R_g$ in dependence of the inclination angle). This effect can lead to the ambiguity of determination of the radius from the blueshift.

coordinate linked with the maximal receding does not differ far from $\frac{\pi}{2}$. With knowledge of the radius of the spot we aspire to estimate the mass of the central black hole. Time analysis is necessary to this. The orbital period of the spot would be determined from the observed periodic temporal variabilities in the spectral line profile.

4.5 Time resolved X-ray spectra

The Fe Kα line really shows appreciable variabilities in some X-ray spectra of AGN (fig 4.10). The changes can be just explained by a presence of a hot spot on the disc.[2] Relatively fast time variability of the spectral line suggests that the illuminated spot subsists at a few R_g from the centre [34]. The orbital time T of the spot depends on the radius r of the spot from the centre and also on the mass of the central black hole M:

$$T \approx \frac{2\pi}{\Omega_{\text{kep}}} = \frac{2\pi}{\sqrt{GM}} r^{\frac{3}{2}}, \tag{4.9}$$

where r and M are now expressed in SI units. Using eq. (3.21) we get a relation, in which the radius R is in units of gravitational radii R_g:

$$T = 2\pi \frac{GM}{c^3} R^{\frac{3}{2}}. \tag{4.10}$$

After putting the values instead of constants we get an arbitrary relation:

$$T \doteq 31.04\, R^{\frac{3}{2}} \frac{M}{10^6 M_\odot}\, \text{s}. \tag{4.11}$$

So, if the time variabilities in our example spectrum (fig 4.8) were observed of order ks, we would be able to estimate the mass of the black hole as $M \approx 10^6 M_\odot$. The determination of the shorter time periods is complicated due to insufficient sensitivity of nowadays X-ray instruments. The critical integration time is about 5ks [35]. Under this value the uncertainty in continuum level would become significant. In [35] the statistical analysis of fig 4.10 was made for the observed Fe Kα line from Seyfert galaxy Mrk766. The authors drew a conclusion that the observed variability corresponds to the sinusoidal changes caused by a circular orbit of a spot with an orbital period 165ks (the smoothed line in the figure). From the energy shift of the spectral line the limit values of the central mass can be estimated. The lower limit of the mass corresponding to the inclination angle

[2] The origin of such a spot can be several. One explanation is due to magnetic reconnections which would illuminate very small areas of the accretion flow [19].

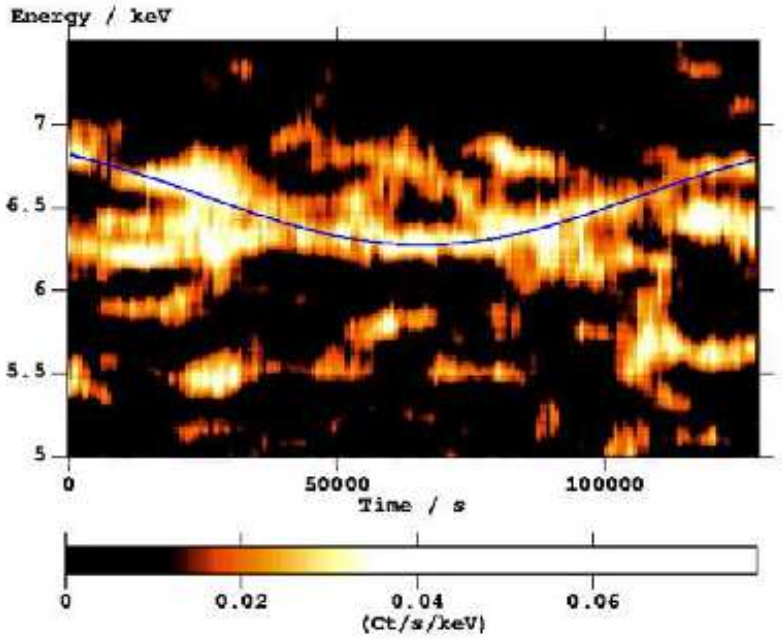

Figure 4.10: Time variability of the energy of the observed Fe Kα line of Mrk 766 (data from XMM Newton). [35]

$\theta = 90$deg is $4.9 \times 10^5 M_\odot$, which restricts the distance of the orbiting spot to a few hundreds of gravitational radii. The upper limit $4.5 \times 10^7 M_\odot$ is derived from the gravitational redshift. The spot would be then persist at $24R_g$ (the absolute distance from the central black hole is then in orders of AU).

4.6 Time evolution of a spectral line

We intend to analyse time evolution of a spectral line profile of the orbiting spot, encouraged by the pioneering observations of time variabilities in the Fe Kα line. From fig 4.11 it is obvious that for some inclined orbit the time delay occur in consequence of that the radiation comes from the differently distant parts of the disc. In the Newtonian approach, the time delay is given by:

$$\delta t = R(1-\cos\varphi)\sin\theta_0. \tag{4.12}$$

The relativistic approximation [23] has the form:

$$\delta t = (R-1)(1-\cos\varphi)\sin\theta_0 + 2\ln\left(\frac{1+\sin\theta_0}{1+\cos\varphi\sin\theta_0}\right). \tag{4.13}$$

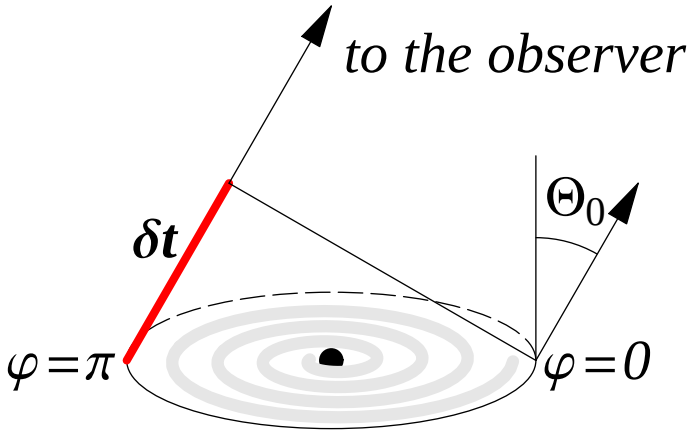

Figure 4.11: Time delay of radiation coming from the different parts of the disc.

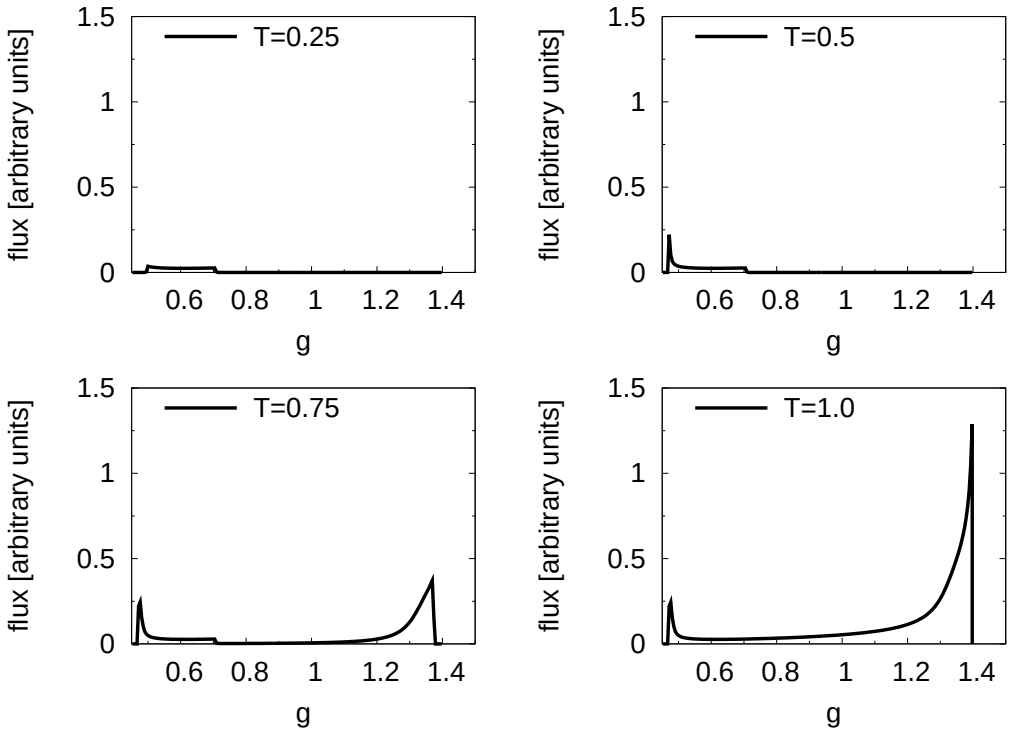

Figure 4.12: Time evolution of an orbiting spot at $R = 6R_g$ with the inclination angle $\theta = 85$deg. The quantity T represents relative part of an orbit of the spot. The orbit is initiated at $\varphi = 0$.

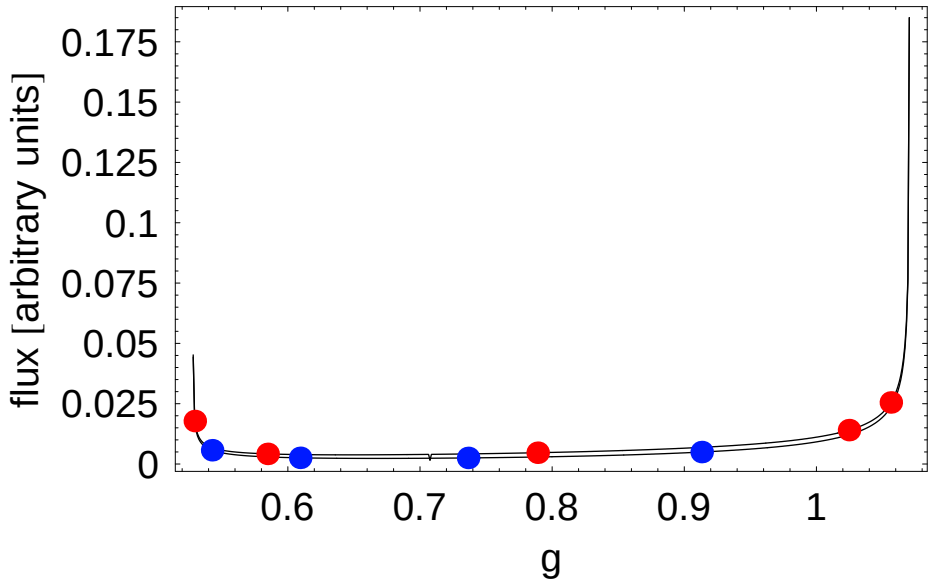

Figure 4.13: Time evolution of an orbiting spot at $R = 6R_g$ with the inclination angle $\theta = 45$deg.

Figure (4.12) illustrates the time evolution of an orbiting spot at $R = 6R_g$ with the inclination angle $\theta = 85$deg. The quantity T labeled in the graphs measures the relative time of the observation. Thus, $T = 0.25$ represents the first quarter of the orbit, $T = 1$ then a whole orbit. The spot begins orbiting at the nearest point to the observer ($\varphi \approx 0$). After a half period (the right upper graph), one could expect that all additions of Doppler longitudinal redshift were already obtained. However, just time delay causes that some addition to the red wing of the line incomes in the second half of the orbit. From eq. (4.13) we can estimate a value of the time delay from the most distant point of the orbit of the mentioned spot:

$$\frac{(\delta t)_{max}}{T_{\rm orbit}} \approx \frac{1}{6}. \tag{4.14}$$

The another expression of the time evolution is due to the marking with the time equidistant tics at the flux-energy graph, as in fig 4.13. The red bullets belong to the front branch of the disc delimited by $\varphi = \varphi_+$ and $\varphi = \varphi_-$ (an illustration in fig 4.14). The blue points appertain to the hind branch of the disc. In the relativistic approach given by eq. (3.27), the azimuthal coordinates, joined with the extremal frequency shifts, are not precisely opposite, thus:

$$\varphi_+ - \varphi_- \neq \pi. \tag{4.15}$$

This inequality has a direct consequence that the front branch of the orbit is longer. Supposing the uniform motion of the spot and steady radiation flux along the orbit,

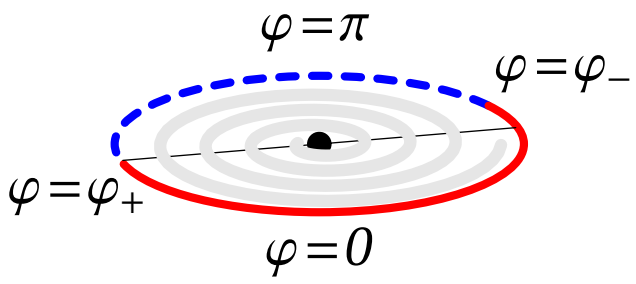

Figure 4.14: An illustration of the disc, which is divided by the extremal azimuthal coordinates $\varphi_\pm$ into the two branches.

more photons are emitted from the front branch. Hence, the red points in fig 4.13 are upwards.

4.7 Gravitational lensing

However, the observations might be inconsistent with the previous conclusion. Especially for the more inclined orbits, when the gravitational lensing significantly increases the intensity of radiation coming from the localities behind the black hole. The front branch is then overstriked by the hind one.

The lensing factor, which enhances the value of the intensity, can be expressed in terms of the relativistic approximation ([23], app. C) as:

$$I_{\text{lens}} = I_0 \left(R + \frac{1-\cos\varphi\sin\theta_0}{1+\cos\varphi\sin\theta_0} \right), \tag{4.16}$$

where the value of I_0 depends also on the mass of the central object. From the expression in the brackets it is obvious that the lensing factor gathers the biggest value for $\varphi = \pi$ $(\cos\varphi = -1)$. It is clear that the lensing effect is transparent for the bigger inclination angles.

The effect of the gravitational lensing is illustrated in fig 4.15. It is appreciable that the hind branch of the orbit (in figure expressed by the blue curve) overruns the front branch after the comprehension of lensing into the computations. To emphasize of the lensing effect the flux on the y-axis is expressed on logarithmic scale. It is obvious from the graphs that the effect of lensing is more remarkable for the more inclined orbits. Also the differences between contributions from both branches are more outstanding for the bigger angles of the inclination.

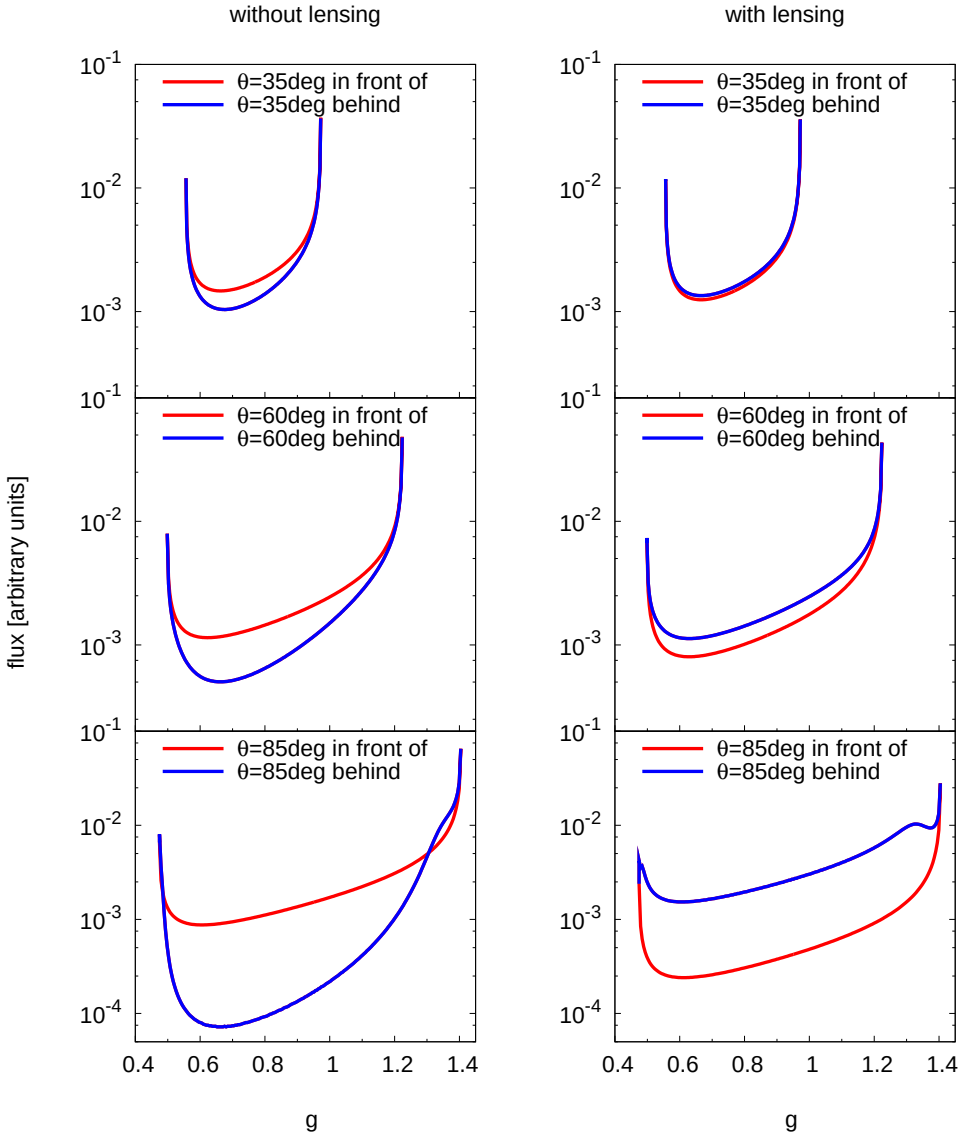

Figure 4.15: The line profile of the spot at $R = 6R_g$ for three different inclination angles, integrated over the front branch (red) and the hind branch (blue) of the orbit. Figures in the left panel do not include lensing, which is counted in profiles in the right panel.

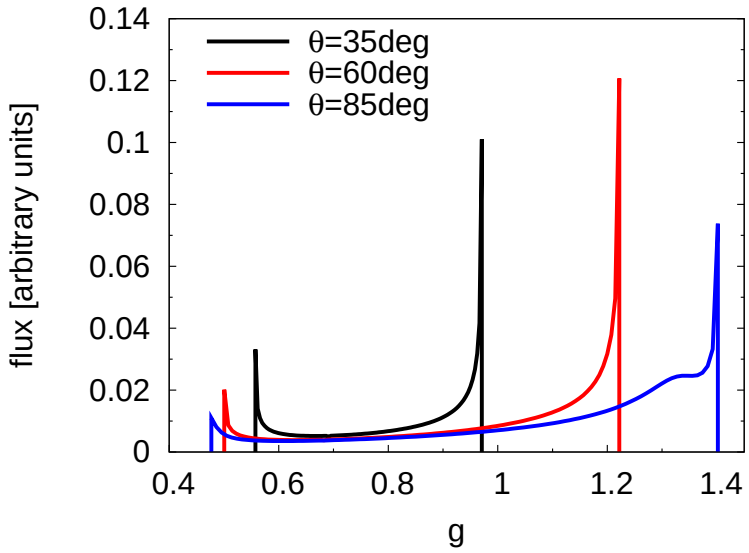

Figure 4.16: The spectral line profiles of radiating rings at $R = 6R_g$ for three angles of the inclination, which include lensing.

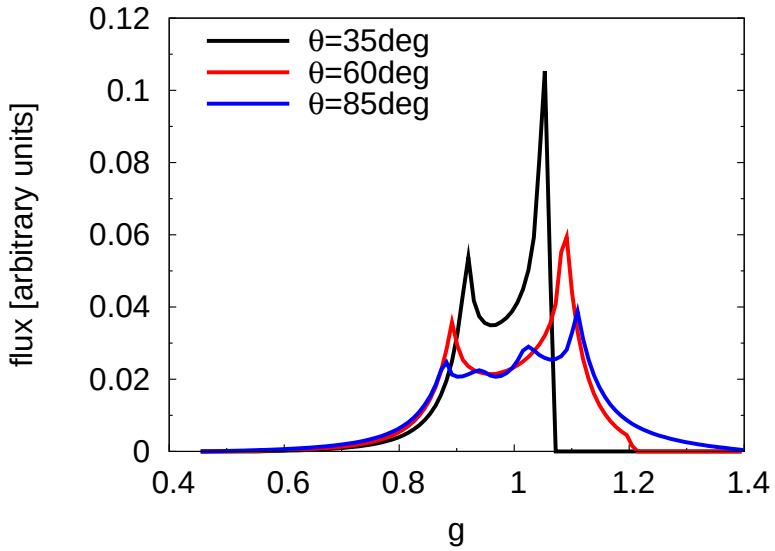

Figure 4.17: The spectral line profiles of accretion discs for three angles of the inclination, which include lensing. The geometrical parameters of the disc are: $q = 2$, $R_{\text{inner}} = 6R_g$, $R_{\text{outer}} = 80R_g$.

As a consequence of lensing, a new horne is able to appear at the spectral line profile, as seen in fig 4.16 (blue curve). The position of the accrued horne is given by the combined effect of the previous course of the profile by eq. (3.15) and lensing. Hence, it occurs at higher frequency compared with the frequency corresponding to radiation coming from the point just behind the black hole.

Also the profiles of discs are markedly influenced by the lensing, and again especially the more inclined. The spectral line profiles of accretion discs including lensing are illustrated in fig 4.17.

4.8 Tracing of the spots in time resolved spectra

In the previous sections we illustrated the relativistic effects acting on photons along their paths in the gravitational field. We considered a presence of a non-axisymmetric emmiting region residing on the disc surface, satisfied by observed time variability of some AGNs, such as in fig 4.10. The resulting time resolved spectral line profiles of accretion discs with a hot spot for different values of the parameters are illustrated in figures 4.18 - 4.27. These calculations already include the time delay and also the gravitational lensing. The chosen parameters of the disc are $q = 2$, $R_{\text{inner}} = 6R_g$, $R_{\text{outer}} = 80R_g$, with an exception in fig 4.28 where $R_{\text{inner}} = 20R_g$. The width of the spot is $w = 0.1R_g$ and its brightness overstrikes $100\times$ the average flux from the surrounding disc (with an exception in fig 4.27, where the brightness is $200\times$ higher than the disc).

Each figure is devided into eight graphs, which represent the spectrum integrated in the strict part of the spot's orbit. The incident spot begins to orbit at $\varphi = 0$. The left upper graph represents the first eighth of the orbit. Contrary to fig 4.12 the second figure corresponds to the second eighth of the orbit etc. In the Newtonian approximation, the most redshift would occur for all inclinations in the interface between the second and the third graph. However in general relativistic approach, the value of the corresponding azimuthal angle is shifted to higher values and the effect is powered by the time delay. The effect of time delay is clearly seen in fig 4.18 ($R = 6R_g$,$\theta = 85$deg). We made an estimation of the maximal time delay of radiation of this spot (eq. 4.14), which is in this case even higher than the integrational time. Hence, in the fourth eighth (left bottom graph) we obtain the maximal redshift instead of turning back of the spot's contribution. In the sixth eighth our detectors are suddenly congested by signal practically from all over the range of shifted frequencies.

A remarkable result appears in fig 4.24. The blue peak linked with the spot occurs between the peaks of the disc. It is a consequence of very strong gravitational redshift relative to the Doppler effect, which causes that the maximal blueshift comes on for further orbits (in this case $\approx 10R_g$) in spite of the fact that

the orbital velocity is maximal for the innermost orbit.

In fig 4.28 we consider a spot orbiting around a black hole at the radius R which is closer than the inner edge of the disc. As a result the peaks joined with the spot are more shifted in frequency than any contribution from the disc.

4.9 The orbit's inclination

In the previous sections we showed, how spectral line profiles vary in dependence upon the value of the inclination angle. Empirically, we can say the more inclination angle the more shifted line and the more different heights of the peaks. Now, we intend to make some quantitative analysis of this. Let introduce two parameters of the shape of the spectral line, as in fig 4.29. The parameter b:

$$b = g_{blue} - g_{\mathrm{red}}, \tag{4.17}$$

which represents the extension of the line, and a parameter p, which is defined as a ratio of the peak's heights:

$$p = \frac{I_{\mathrm{red}}}{I_{\mathrm{blue}}} = \left(\frac{g_{\mathrm{red}}}{g^3_{\mathrm{blue}}}\right)^3 \in \langle 0,1\rangle\,, \tag{4.18}$$

The quantity g_{red} (resp. g_{blue}) are linked with the red horne (resp. blue horne). In the case of a spot the peaks occur at the wings of the spectral line and the values of g_{red} and g_{blue} correspond to the extremal shifts:

$$g_{\mathrm{red}} \approx g_-,\ \ g_{\mathrm{blue}} \approx g_+. \tag{4.19}$$

We already have the equations (3.29) - (3.34), which describe the relation between the extremal shift $g_\pm$ and the geometry (R,θ). To the rough estimations, we set again:

$$\varphi_- \approx \frac{\pi}{2},\ \ \varphi_+ \approx \frac{3}{2}\pi. \tag{4.20}$$

We get:

$$g_\pm = \frac{\sqrt{R(R-3)}}{R \mp \sqrt{R+2}\sin\theta}. \tag{4.21}$$

Thus,

$$b \approx \sqrt{R(R-3)}\left(\frac{1}{R-\sqrt{R+2}\sin\theta} - \frac{1}{R+\sqrt{R+2}\sin\theta}\right). \tag{4.22}$$

After transfer on the common denominator:

$$b \approx 2\sqrt{R(R+2)(R-3)}\frac{\sin\theta}{R^2-(R+2)\sin^2\theta}. \tag{4.23}$$

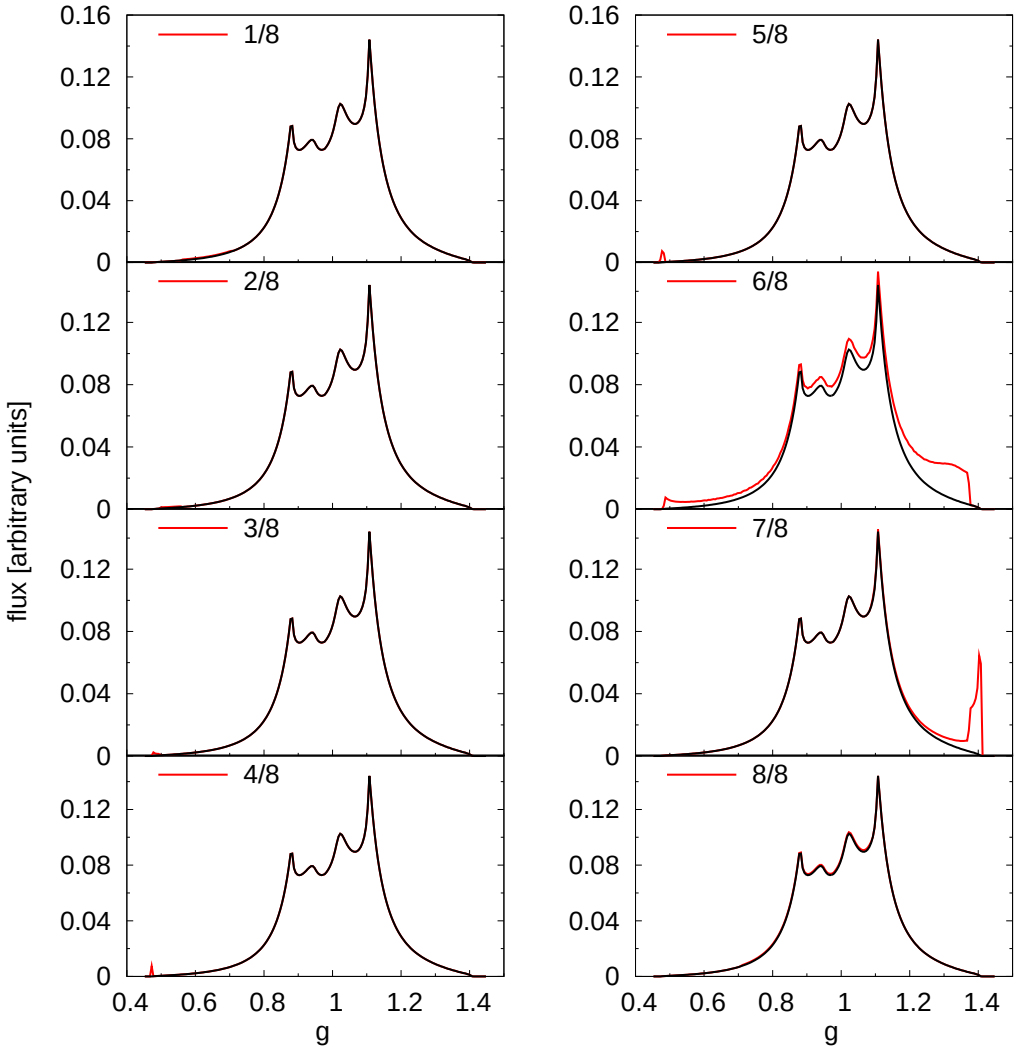

Figure 4.18: The spectral line profile of an accretion disc with the inclination $\theta = 85$deg with a hot spot residing at $R = 6R_g$ on its surface.

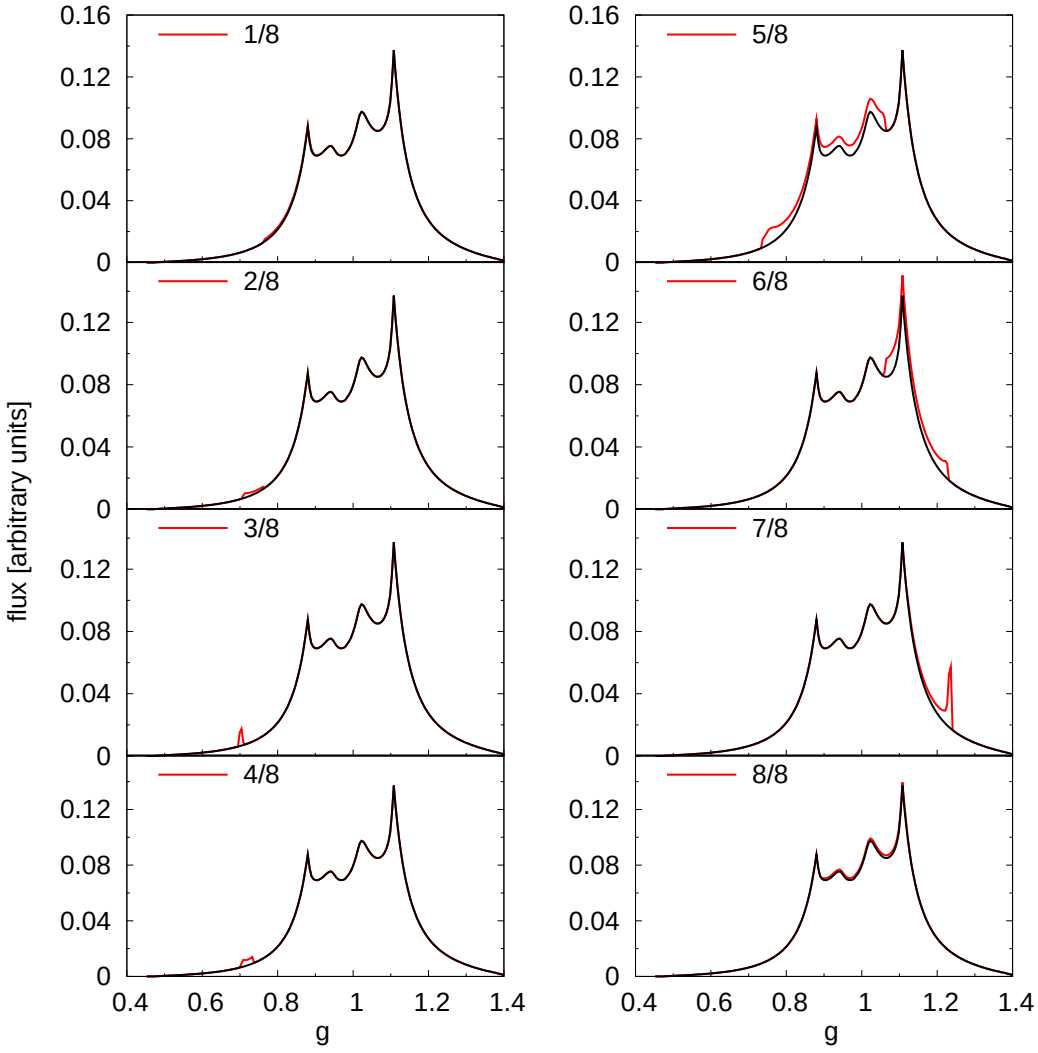

Figure 4.19: The spectral line profile of an accretion disc with the inclination $\theta = 85$deg with a hot spot residing at $R = 15R_g$ on its surface.

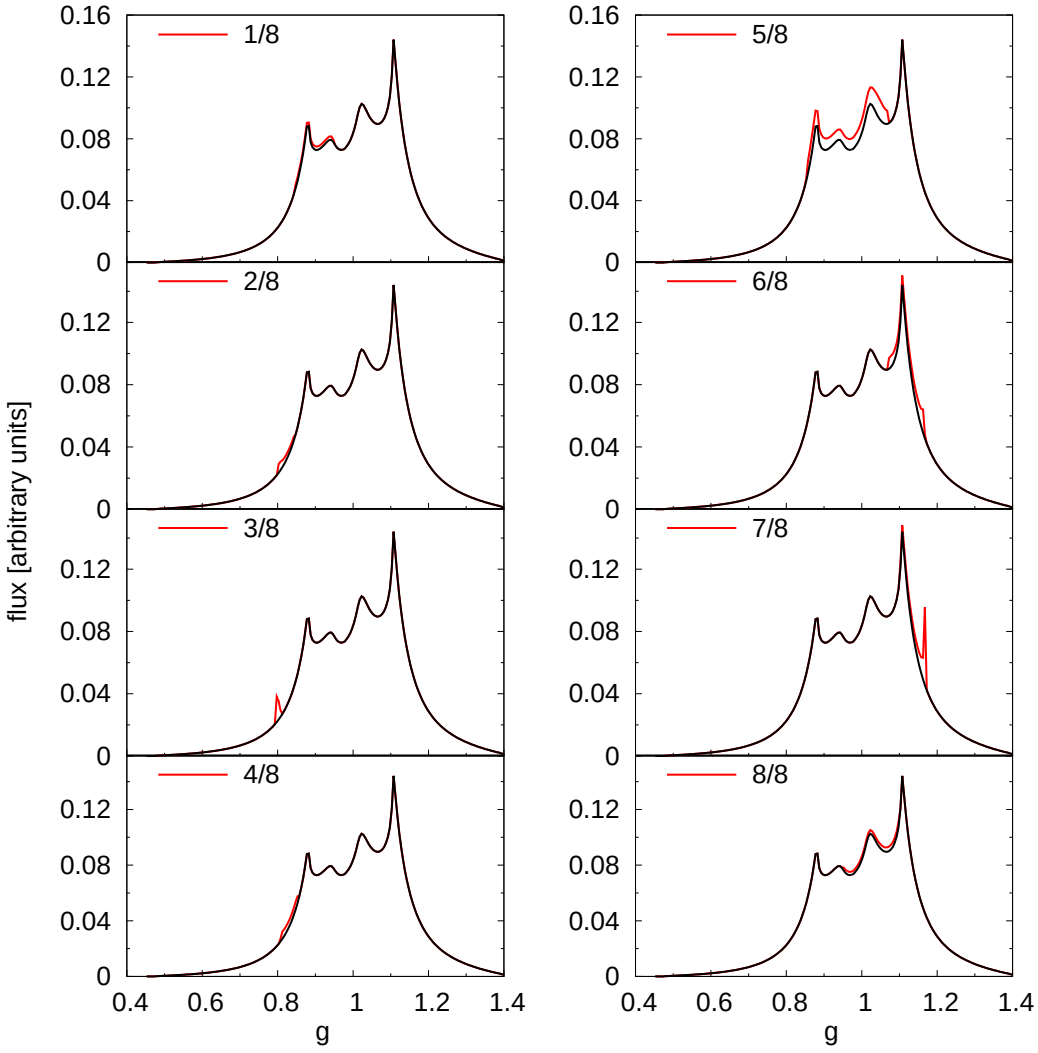

Figure 4.20: The spectral line profile of an accretion disc with the inclination $\theta = 85$deg with a hot spot residing at $R = 30R_g$ on its surface.

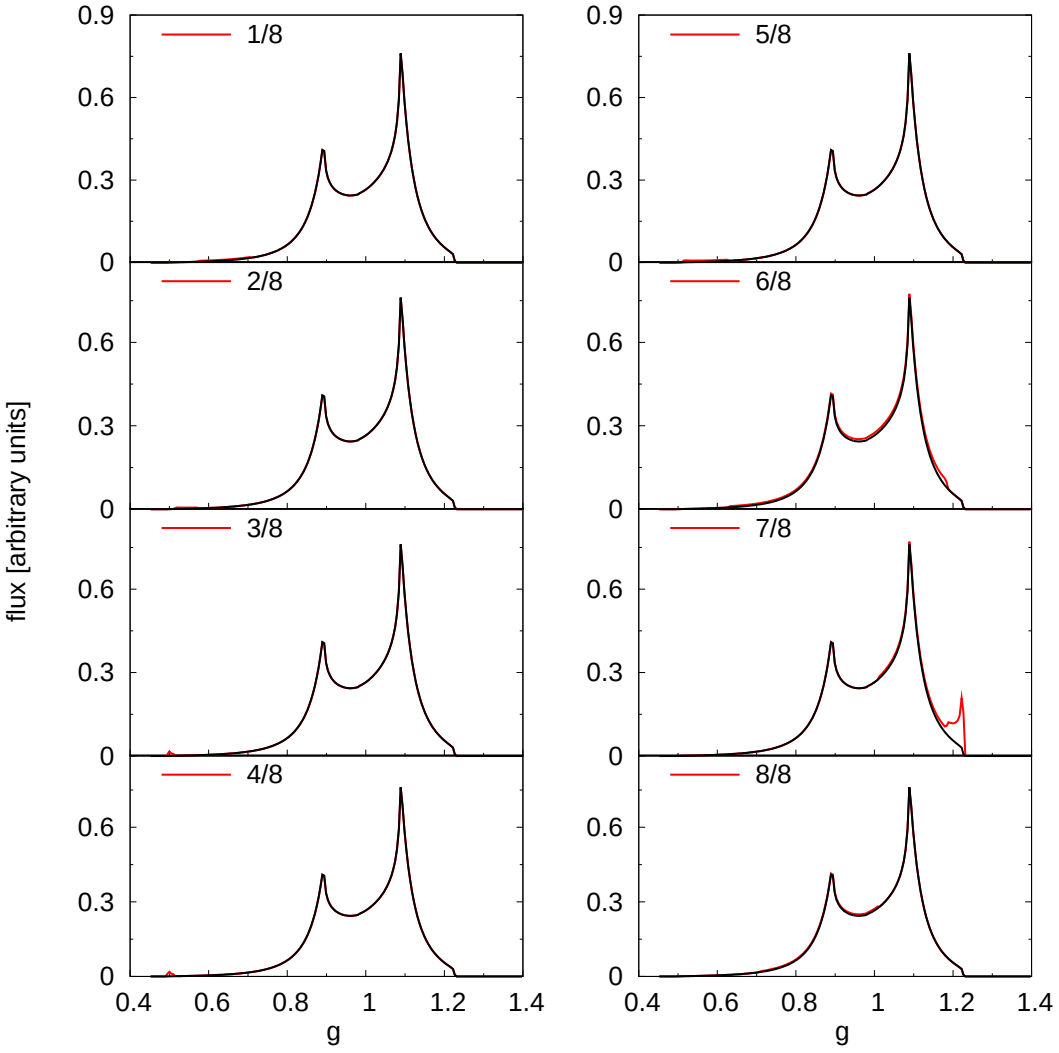

Figure 4.21: The spectral line profile of an accretion disc with the inclination $\theta = 60$deg with a hot spot residing at $R = 6R_g$ on its surface.

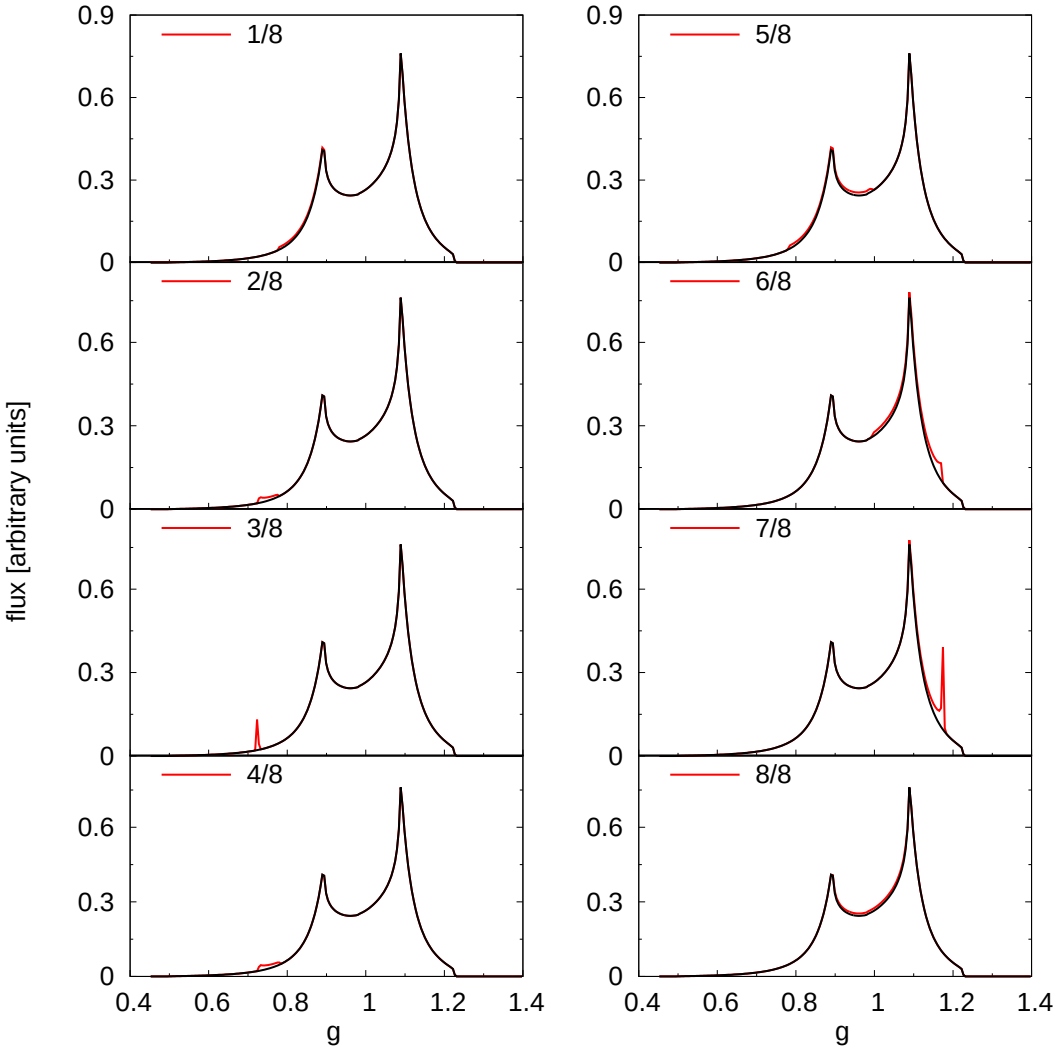

Figure 4.22: The spectral line profile of an accretion disc with the inclination $\theta = 60$deg with a hot spot residing at $R = 15R_g$ on its surface.

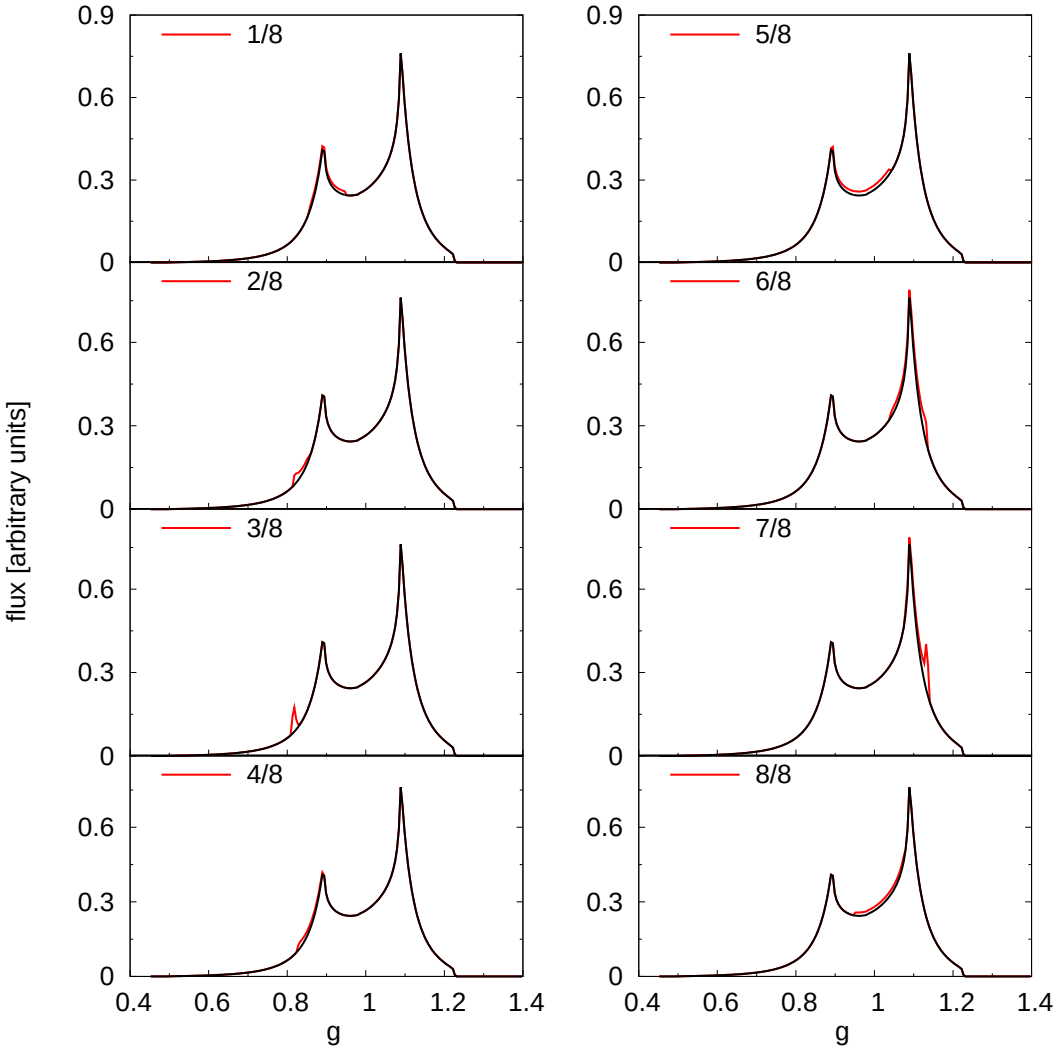

Figure 4.23: The spectral line profile of an accretion disc with the inclination $\theta = 60$deg with a hot spot residing at $R = 30R_g$ on its surface.

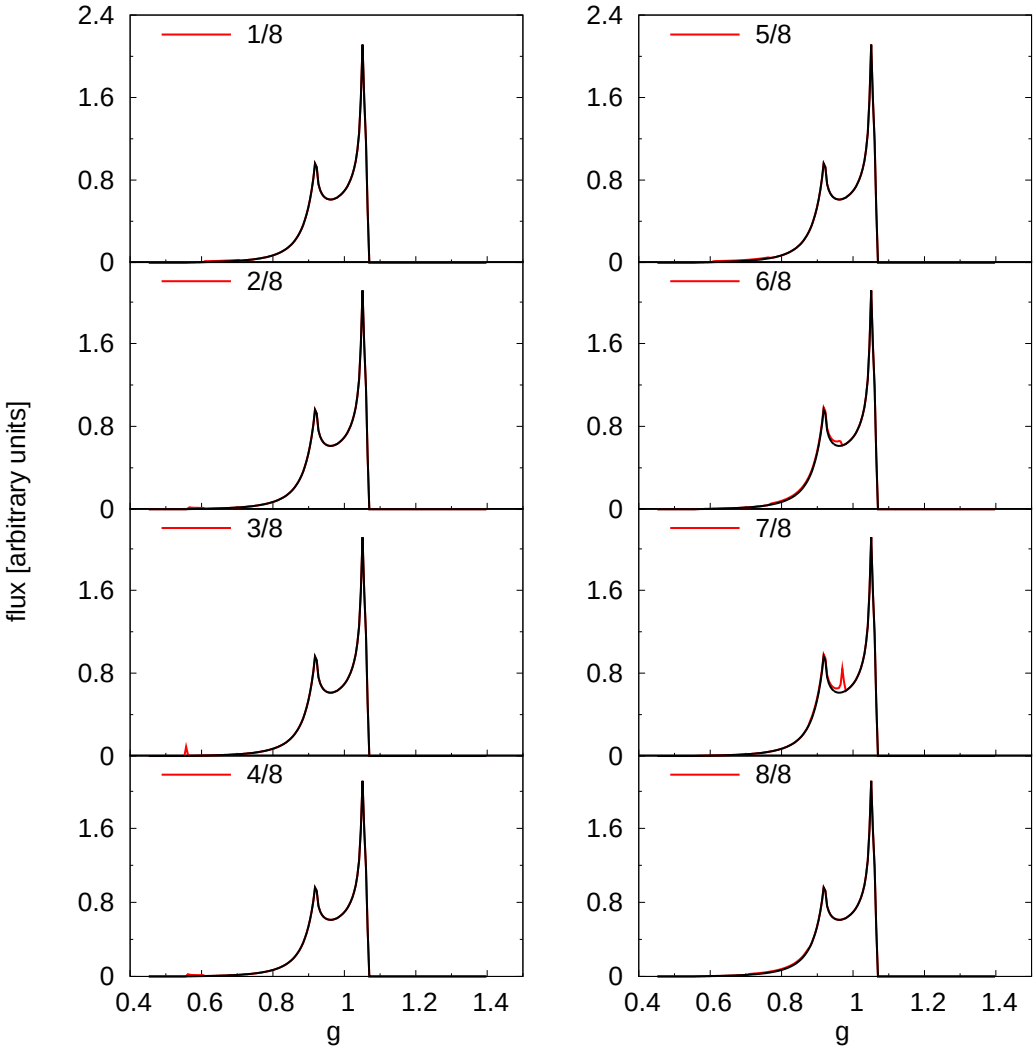

Figure 4.24: The spectral line profile of an accretion disc with the inclination $\theta = 35$deg with a hot spot residing at $R = 6R_g$ on its surface.

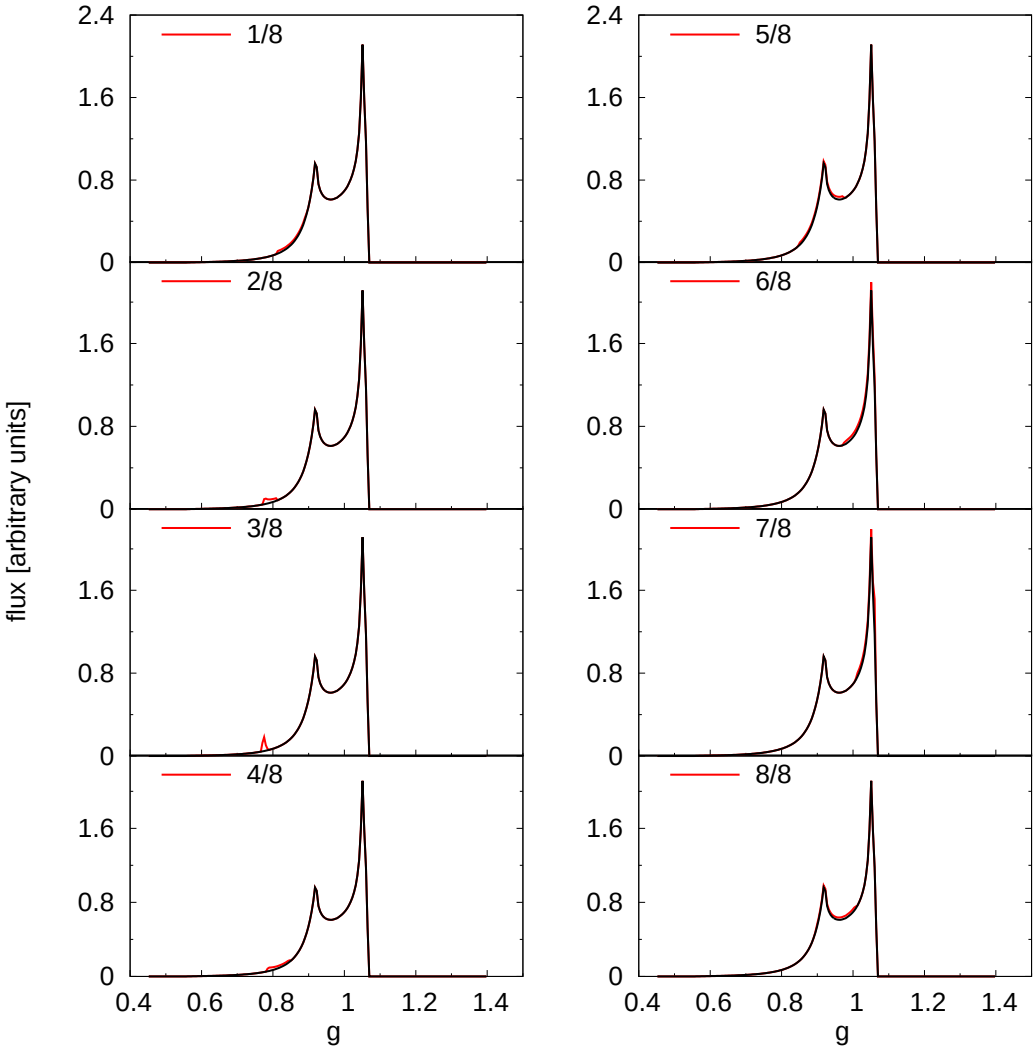

Figure 4.25: The spectral line profile of an accretion disc with the inclination $\theta = 35$deg with a hot spot residing at $R = 15R_g$ on its surface.

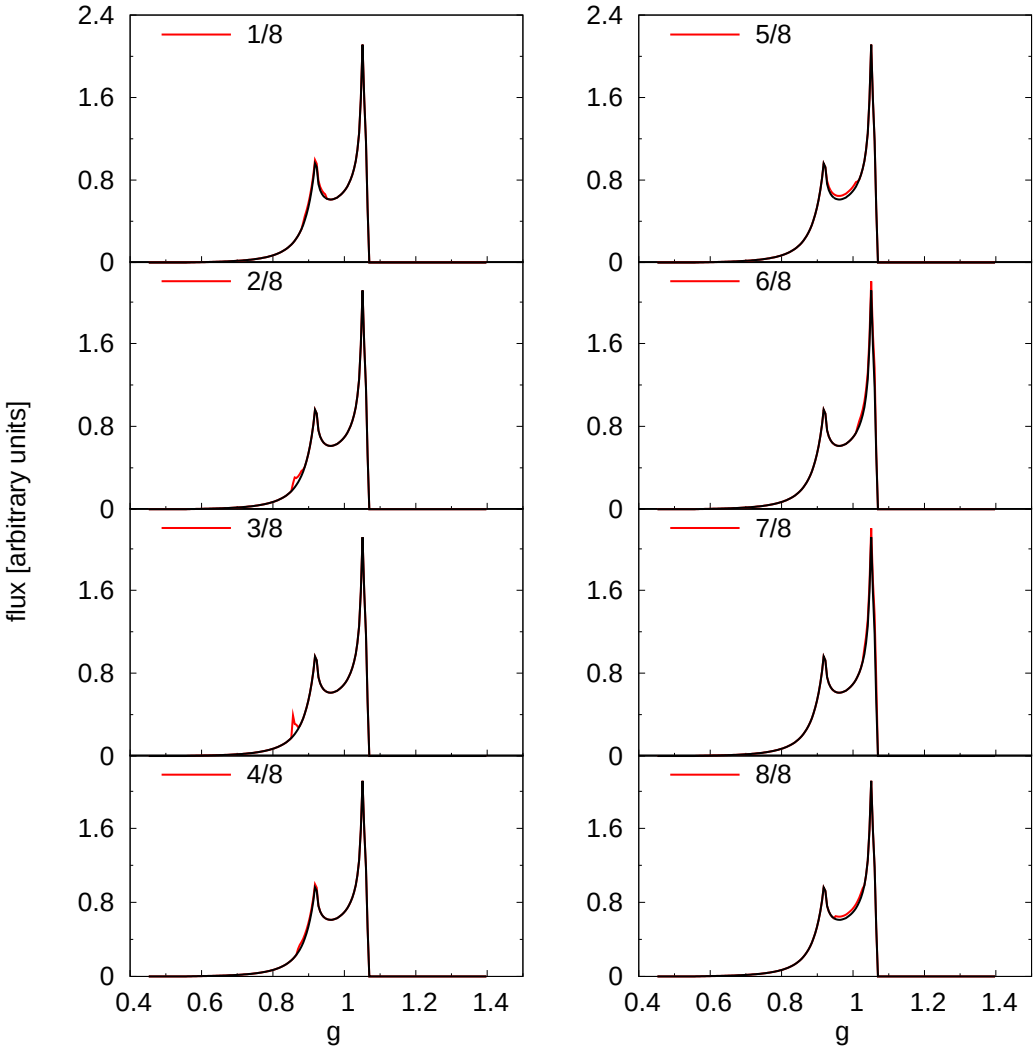

Figure 4.26: The spectral line profile of an accretion disc with the inclination $\theta = 35$deg with a hot spot residing at $R = 30R_g$ on its surface.

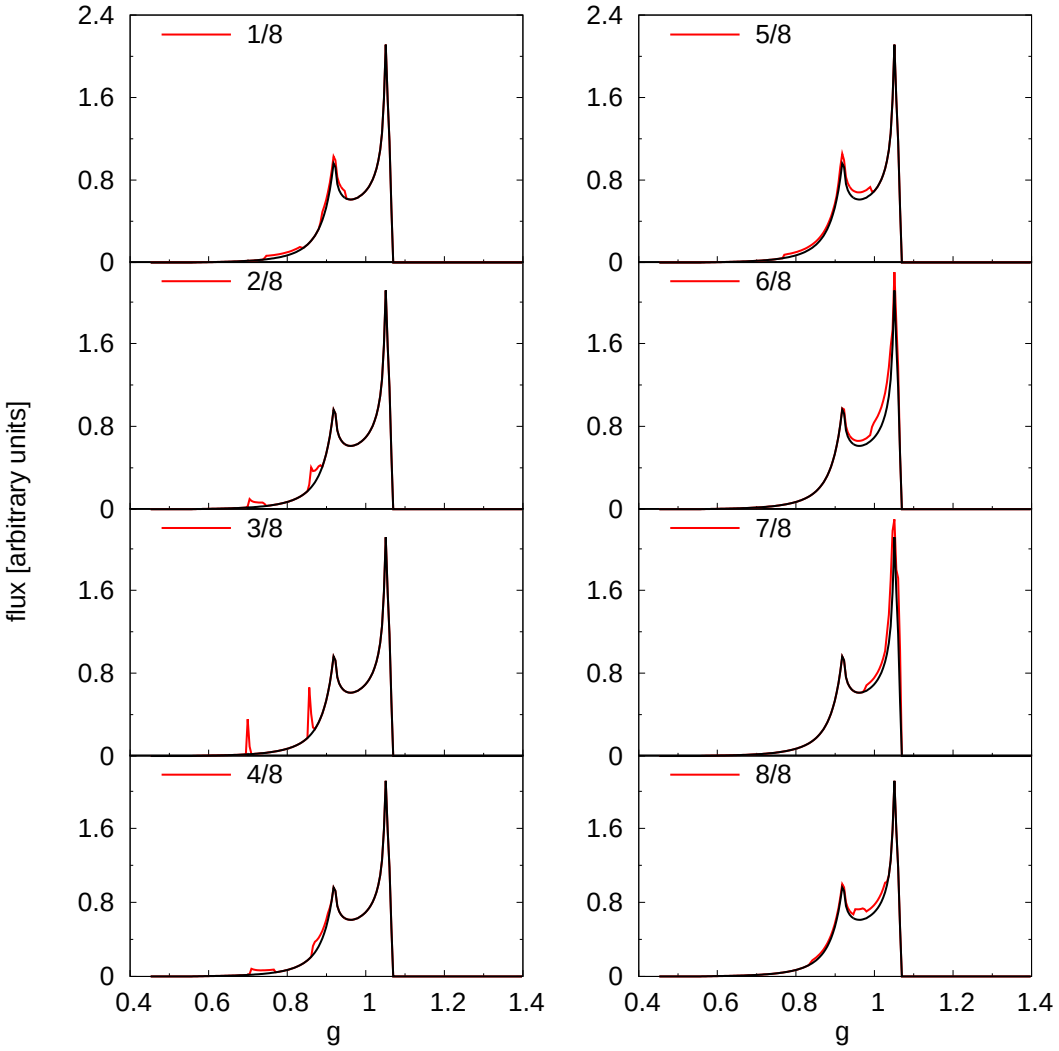

Figure 4.27: The spectral line profile of an accretion disc with the inclination $\theta = 35$deg with two hot spots residing at $R = 10R_g$ and $R = 30R_g$ on its surface.

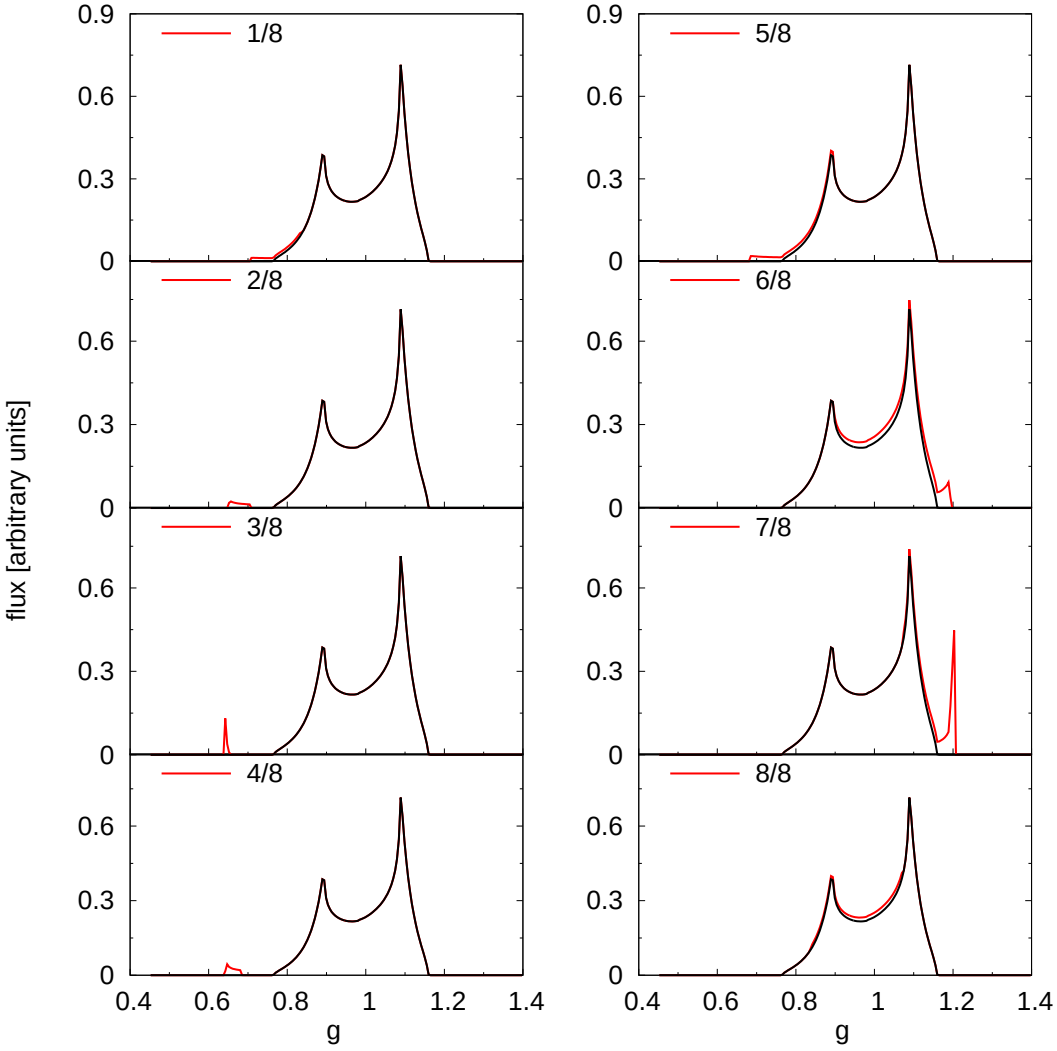

Figure 4.28: The spectral line profile of an accretion disc with the inclination $\theta = 60$deg with a hot spot orbiting at $R = 6R_g$, while the inner edge of the disc is $R = 20R_g$.

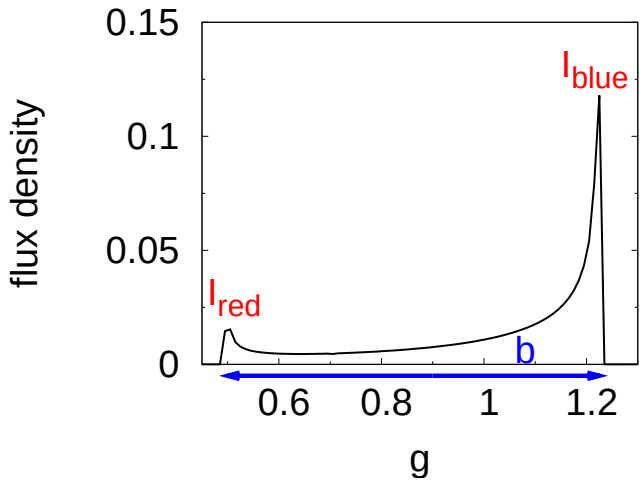

Figure 4.29: An illustrational figure of a broadened spectral line.

The limit for $R \gg 1$ gives:

$$b \approx \frac{2}{\sqrt{R}} \sin\theta. \tag{4.24}$$

For small inclinations we get very simple linear dependence:

$$b \approx \frac{2}{\sqrt{R}} \theta. \tag{4.25}$$

In the same way we can approximate the relation for p:

$$\sqrt[3]{p} = \frac{R - \sqrt{R+2}\sin\theta}{R + \sqrt{R+2}\sin\theta} = \frac{\frac{R}{\sqrt{R+2}} - \sin\theta}{\frac{R}{\sqrt{R+2}} + \sin\theta}. \tag{4.26}$$

Thus:

$$p = \left(\frac{\frac{R}{\sqrt{R+2}} - \sin\theta}{\frac{R}{\sqrt{R+2}} + \sin\theta} \right)^3. \tag{4.27}$$

The figures 4.30 and 4.32 express the dependency of the parameters on the inclination angle for a constant R. Red curves in the graphs represent the approximative formulas derived above (equations 4.24 and 4.27). The dependencies on the value of the radius R are illustrated in fig 4.31 and fig 4.33 for some chosen values of R.

It is clear from the graphs that both parameters, b and p, are increasing functions of the inclination angle. The course of the dependencies is slower for more distant orbits, as seen in fig 4.31 and fig 4.33. The approximative formulas derived above are consistent with the numerical calculations and are suitable in particular for smaller angles of the inclination or bigger values of the radius R.

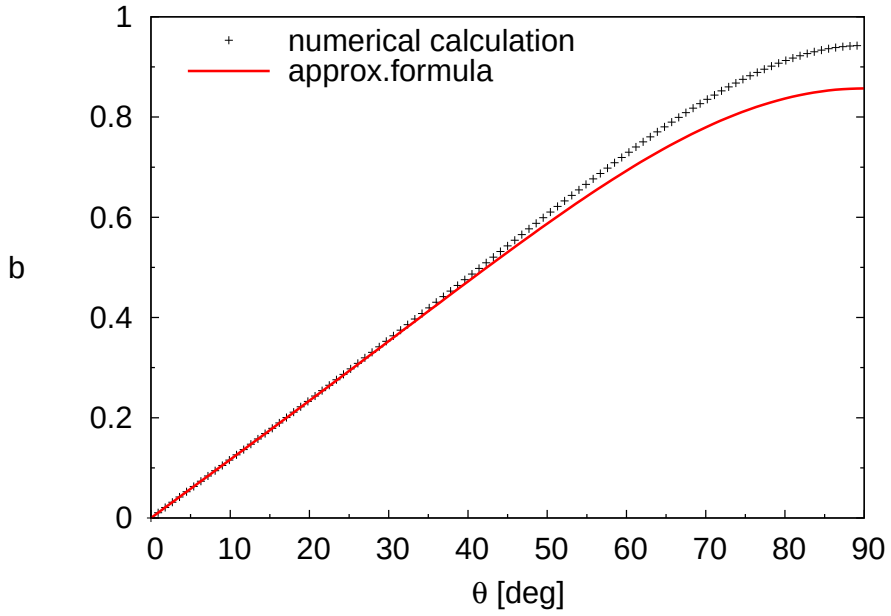

Figure 4.30: The dependency of the maximal broadening b of a spectral line of an orbiting spot at $R = 6R_g$ on the inclination angle θ.

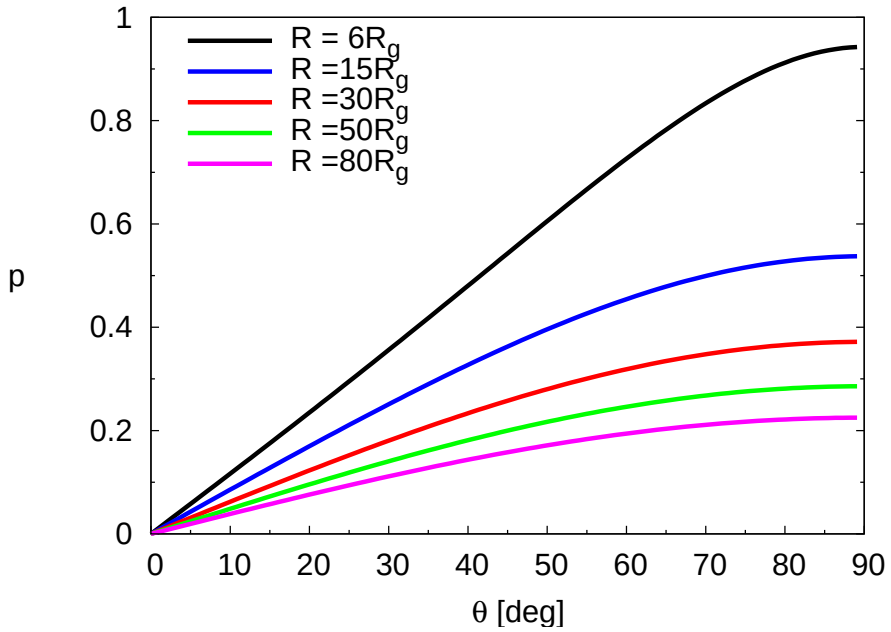

Figure 4.31: The dependency of the maximal broadening b of a spectral line on the inclination angle θ depending on the value of radius R.

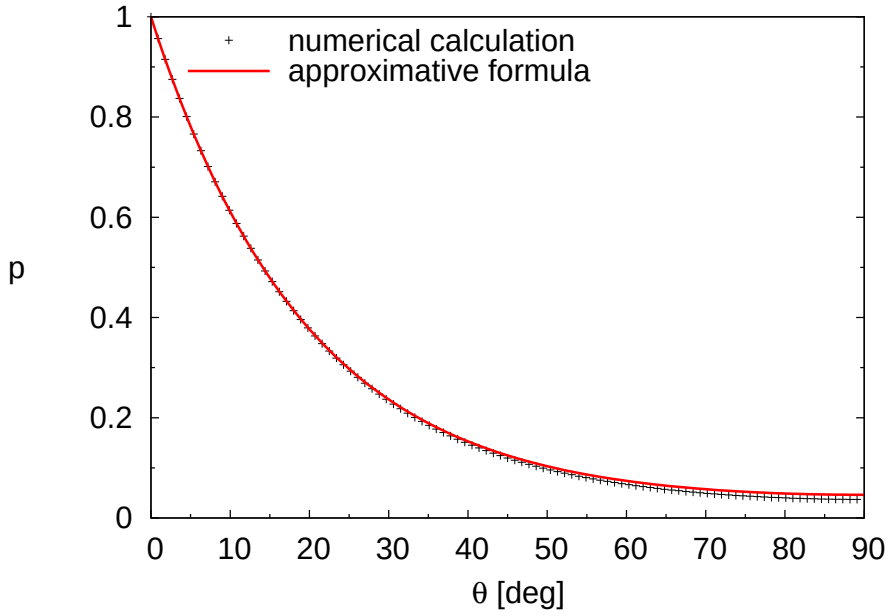

Figure 4.32: The dependency of the ratio of the peak's heights p of a spectral line of an orbiting spot at $R = 6R_g$ on the inclination angle θ.

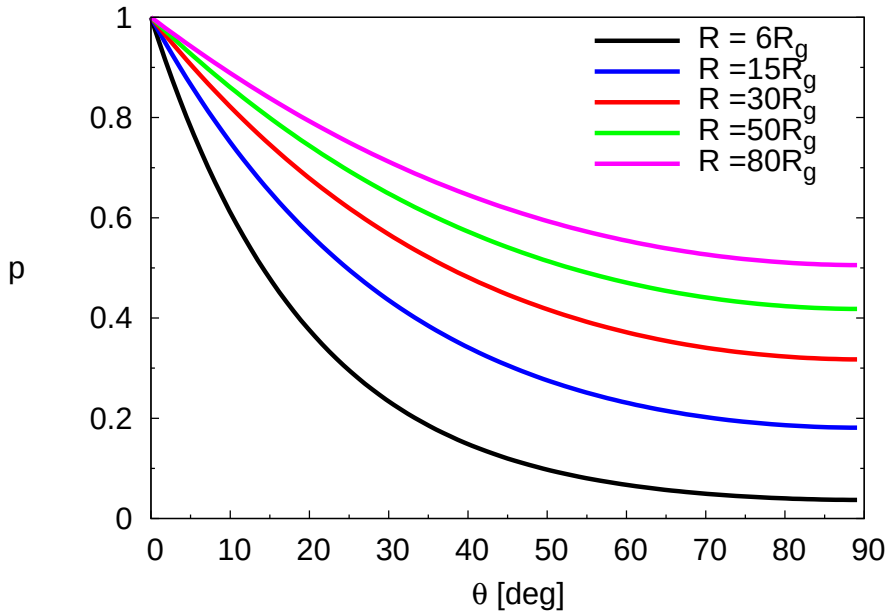

Figure 4.33: The dependency of the ratio of the peak's heights p of a spectral line on the inclination angle θ depending on the value of radius R.

Chapter 5

Conclusions

We followed an explanation of the observed distorted profile of a narrow spectral line (Fe Kα line) due to very fast orbital velocity and presented strong gravity field, which occur via an accretion disc around a compact object. We produced a toy-model for computations of the spectral line profiles in general relativistic approach.

The computed spectral line profiles of axially symmetric radiating rings and accretion discs are illustrated in fig 4.3-4.7. The common characteristic feature is an asymmetric double-horned profile. The frequency shift, the ratio of the heights of the peaks, time delay of the signal and distortion due to lensing effect are functions of the radius from the centre and the inclination angle. The profile is the more influenced the closer to black hole the signal comes from and the bigger is the inclination angle.

Further, we presented the profiles with a contribution of the non-axisymmetric radiating area residing on the disc surface. The procedure, how to determine the orbital radius R of such a spot from the spectral line profile, was shown in section 4.4. The continually progressive spectral resolution of the measurements gives us the reason for deal with the time dependent spectra and to trace the spots in the spectral line profiles, fig 4.18 - fig 4.27. The relation between the shape of the spectral line profile and the inclination angle was discussed in 4.9.

We pursued the analysis only of a spectral line profile after subtracting the continuum level. A possible extension of this work is to study time variabilities in the spectral line within the context of changes in the continuum level. The natural extension of our work is to apply the model on observational data (especially after obtaining data from the more sensitive detectors) and to generalize calculations for Kerr's metric and the presented magnetic field.

Appendix A

Details of numerical calculations

All figures of the predicted profiles of a spectral line are in fact histograms. In numerical calculations we are practically not restricted in the choice of the number of bars, compared with the observational detectors. The maximal count of frequency channels is given by the spectral resolution of the measurement. In our study of a relativistic spectral line profile we keep mainly the Fe Kα line in mind. The intrinsic frequency of this line is 6.4keV. The spectral resolution of nowadays instruments is expressed in fig A.1. In the energy range of the Fe Kα line:

$$dE_{FWHM} \approx 10\text{eV}. \tag{A.1}$$

The broadening parameter of our models of the spectral line profiles due to Doppler and gravitational shifts does not overreach a value of one nor for the extremal radius R in Schwarzschild metric (fig 4.31). In terms of energies it means that the maximal extension is about 6keV. This gives a maximal value of the number of channels $N_{\max} \approx 600$. In order to maintain an adequate level of the ratio of signal to noise and in an effort to have smoothed profiles, the number of channels has to be reduced. In our computations we put $N = 200$.

The other parameters of numerical calculations are the integrational steps. We put $\mathrm{d}R = 0.05$ and $\mathrm{d}\varphi \approx 10^{-4}$ for computations of profiles of the most extended discs, in the other cases the same or better resolution.

The y-values of the graphs are normalized in the sense that the sum of all contribution from energy channels gives one (the exceptions are the graphs, which demonstrate contributions of a spot from a part of its orbit).

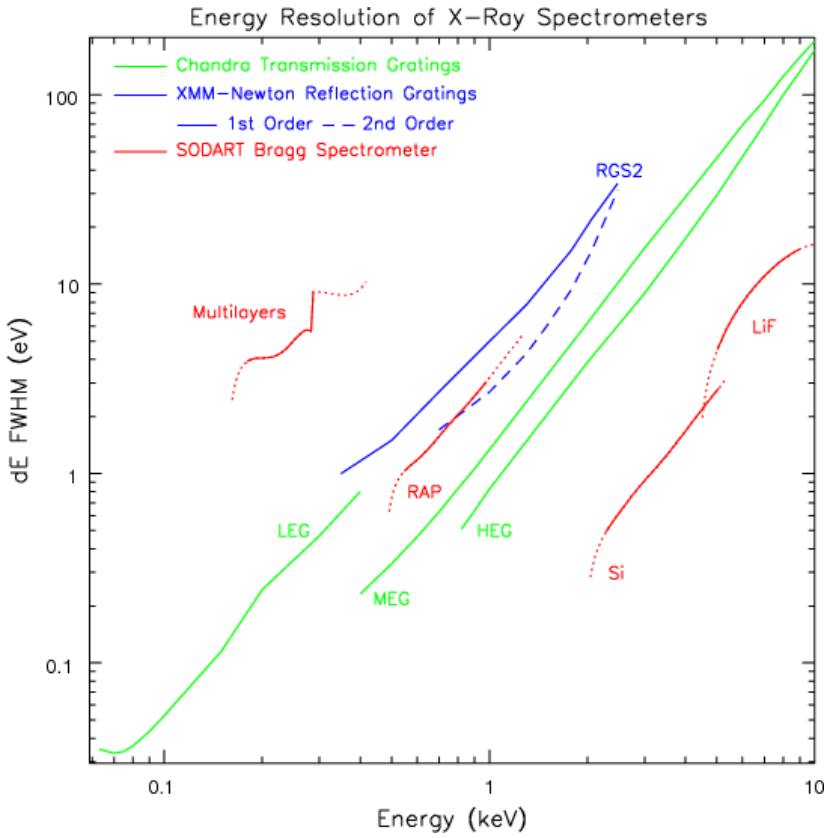

Figure A.1: The energy resolution of nowadays detectors (from *hea-www.harvard.edu*).

Appendix B

Aproximation of time delay

Time of flight of photons in the vicinity of the black hole is strongly influenced by the presented gravitational field. The approximation used in eq. (4.13) derived in [3, 23] ensues from the Shapiro's approach [30] and is generalized for stronger gravitational fields. From normalization of photon's four-momentum ($p^\mu p_\mu = 0$) and from conservation laws it follows:

$$\mathrm{d}t = 2\frac{1}{(1-u)u^2\sqrt{1-(1-u)u^2b^2}}\mathrm{d}u, \tag{B.1}$$

where $u = 2/r$, and $b = \lambda/2$ is a dimensionless impact parameter. The integration of (B.1) leads to an elliptic integral. The integrand can be rearranged in a more suitable form:

$$\int \frac{1}{(1-u)u^2\sqrt{1-(1-u)u^2b^2}}\mathrm{d}u = -\frac{\sqrt{1-(1-u)u^2b^2}}{u}$$
$$+\frac{b^2}{2}\int \frac{u}{\sqrt{1-(1-u)u^2b^2}}\mathrm{d}u + \int \frac{1}{(1-u)u\sqrt{1-(1-u)u^2b^2}}\mathrm{d}u. \tag{B.2}$$

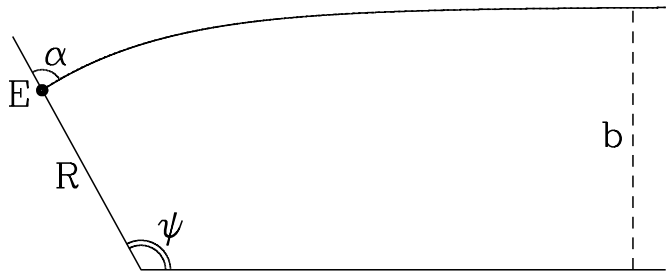

Figure B.1: Example photon trajectory (from [3]).

In terms of the approximation in [3]:

$$1-\cos\alpha = (1-\cos\psi)\left(1-\frac{2}{r}\right), \tag{B.3}$$

the first item of the right hand side of eq. (B.2) can be reexpressed as $-\cos\alpha/u$ and the remaining integrals can be expanded in $x \equiv (1-\cos\alpha)/(1-u)$.

Then, the terms with the same power of u can be collected together. From the approximation till the first order of u follows:

$$T_j = -r\cos\psi_j - (1-\cos\psi_j) - 2\log\left(\frac{1+\cos\psi_j}{2}\right), \tag{B.4}$$

where $j = 1,2$ and $\cos\psi_1 = \sin\theta$, $\cos\psi_2 = \sin\theta\cos\varphi$.

Then,

$$\delta t(r,\varphi,\theta) = T_2 - T_1. \tag{B.5}$$

After some arrangements we obtain:

$$\delta t = (R-1)(1-\cos\varphi)\sin\theta_0 + 2\ln\left(\frac{1+\sin\theta_0}{1+\cos\varphi\sin\theta_0}\right). \tag{B.6}$$

Appendix C

Aproximation of lensing

The concentration of radiation intensity by lensing can be described due to contraction of the solid angle. The observational flux is then proportional to the element area expressed in terms of the source coordinates:

$$b\mathrm{d}b\mathrm{d}\varphi' = b\left|\frac{\partial(b,\varphi')}{\partial(r,\varphi)}\right|\mathrm{d}r\mathrm{d}\varphi = b\frac{\partial b}{\partial r}\frac{\partial\varphi'}{\partial\varphi}\mathrm{d}r\mathrm{d}\varphi. \tag{C.1}$$

The impact parameter b is connected with emission angle α by the equation:

$$\sin\alpha = \frac{b}{r}\left(1-\frac{2M}{r}\right). \tag{C.2}$$

From the Beloborodov's approximation it follows:

$$1-\cos^2\alpha = \left[2-(1-\cos\psi)\left(1-\frac{2M}{r}\right)\right](1-\cos\psi)\left(1-\frac{2M}{r}\right), \tag{C.3}$$

where

$$\cos\psi = \cos\varphi\sin\theta. \tag{C.4}$$

Combining these two equations we obtain:

$$b^2 = r^2(1-\cos\psi)\left[2-(1-\cos\psi)\left(1-\frac{2M}{r}\right)\right]. \tag{C.5}$$

Differentiating this relation we get:

$$\begin{aligned} b\frac{\partial b}{\partial r} &= r(1-\cos\psi)\left[2-(1-\cos\psi)\left(1-\frac{2M}{r}\right)\right]-M(1-\cos\psi)^2 \\ &= \left[r+M\frac{1-\cos\psi}{1+\cos\psi}\right]\sin^2\psi. \end{aligned} \tag{C.6}$$

Applying by the sine and cosine theorems we obtain:

$$\sin\varphi' = \frac{\sin\varphi}{\sin\psi}, \tag{C.7}$$

$$\cos\varphi' = \frac{\cos\varphi\cos\theta}{\sin\psi}. \tag{C.8}$$

From the first equation we get:

$$\cos\varphi'\frac{\partial\varphi'}{\partial\varphi}\sin\psi + \sin\varphi'\frac{\partial}{\partial\varphi}\sin\psi = \cos\varphi. \tag{C.9}$$

From eq. (C.4) follows:

$$\frac{\partial}{\partial\varphi}\sin\psi = \frac{\partial}{\partial\varphi}\sqrt{1-\sin^2 i\cos^2\varphi} = \frac{\sin^2 i\sin\varphi\cos\varphi}{\sin\psi}. \tag{C.10}$$

Combining these equations we finally obtain:

$$\frac{\partial\varphi'}{\partial\varphi} = \frac{\cos i}{\sin^2\psi}, \tag{C.11}$$

and the resulting formula for the area element is then given by:

$$b\mathrm{d}b\mathrm{d}\varphi' = \left[r + M\frac{1-\cos\psi}{1+\cos\psi}\right]\cos i\mathrm{d}r\mathrm{d}\varphi. \tag{C.12}$$

The intensity enhanced by lensing can be written as:

$$I_{\mathrm{lens}} = I_0 b\mathrm{d}b\mathrm{d}\varphi'. \tag{C.13}$$

Substituting from eq. (C.12) and pushing of M into I_0 we obtain:

$$I_{\mathrm{lens}} = I_0\left(R + \frac{1-\cos\varphi\sin\theta_0}{1+\cos\varphi\sin\theta_0}\right), \tag{C.14}$$

where the radius R is now expressed in units of R_g.

Bibliography

[1] Adam J. (1990): Line formation in accretion disks, *A&A*, 240, 541

[2] Balbus S. A., Hawley J. F. (1998): Instability, turbulence and enhanced transport in accretion disks, *Rev.Mod.Phys.*, 70, 1

[3] Beloborodov A.M. (2002): Gravitational Bending of Light Near Compact Objects, *A&A*, 586, L85

[4] Chandrasekhar S. (1992): The Mathematical Theory of Black holes, Oxford Univ.Press, New York

[5] Cunningham C.T., Bardeen J.M. (1973): The Optical Appearance of a Star Orbiting an Extreme Kerr Black Hole, *A&A*, 183, 273

[6] Done C. (2001): Galactic Black Hole Binary Systems, *Adv.SpaceRes.*, 28, 255

[7] Dovčiak M., Bianchi S., Guainazzi M., Karas Vl., Matt G. (2004): Relativistic spectral features from X-ray illuminated spots and the measure of the black hole mass in AGN, *MNRAS*, 350, 745

[8] Dovčiak M. (2004): Radiation of Accretion Discs in Strong Gravity, *PhD thesis*, Faculty of Mathematics and Physics, Charles University, Prague

[9] Dove J. B., Wilms J., Begelman M. C. (1997): A self-consistent thermal accretion disk corona model for compact objects, *A&A*, 487, 747

[10] Fabian A. C., Rees M. J., Stella L., White N. E. (1989): X-ray fluorescence from the inner disc in Cygnus X-1, *MNRAS*, 238, 729

[11] Fabian A. C. (2005): X-ray reflections of AGN, *astro-ph*/0511537

[12] Frank J., King A. R., Raine D. J. (1985): Accretion power in astrophysics, University Press, Cambridge

[13] Galeev A. A., Rosner R., Vaiana G. S. (1979): Structured coronae of accretion disks, *A&A*, 229, 318

[14] Georg I. M.,Fabian A. C. (1991): X-ray reflection from cold matter in Active Galactic Nuclei and X-ray binaries, *MNRAS*, 249, 352

[15] Gerbal D., Pelat D. (1980): Profile of a Line Emitted by an Accretion Disk. Influence of the Geometry upon its Shape Parameters, *A&A*, 95, 18

[16] Karas Vl. (1996): Astrophysical Analogies: From Quasars to Pulsars, *lecture text*, Faculty of Mathematics and Physics, Charles University, Prague

[17] Landau L. D., Lifshitz E. M. (1959): Fluid mechanics, Pergamon, Elmsford, New York

[18] Marsch T. R. and Horne K. (1988): Images of accretion discs - II. Doppler tomography, *MNRAS*, 235, 269

[19] Merloni, A. and Fabian, A.C. (2001): Thunderclouds and accretion discs: a model for the spectral and temporal variability of Seyfert 1 galaxies,*MNRAS*, 328, 958

[20] Misner C.W., Thorne K.S., Wheeler J.A. (1973): Gravitation, Freeman, San Francisco

[21] Nandra K., Pounds K.A., Stewart G. C., Fabian A. C., Rees M. J. (1989): Detection of iron features in the X-ray spectrum of the Seyfert I galaxy MCG-6-30-15, *MNRAS*, 236, 39

[22] Pecháček T., Dovčiak M., Karas Vl., Matt G. (2005): The relativistic shift of narrow spectral features from black-hole accretion discs, *A&A*, 441, 855

[23] Pecháček T., Dovčiak M., Karas Vl. (2005): The relativistic shift of spectral lines from black-hole accretion discs, in *RAGtime6/7 Proceedings*, Hledík & Stuchlík (2005), pp. 137

[24] Pounds K. A., Nandra K., Stewart G. C., George I. M., Fabian A. C. (1990): X-ray reflection from cold matter in the nuclei of active galaxies, *Nat*, 344, 132

[25] Reynolds C.S., Nowak M.A. (2003): Fluorescent iron lines as a probe of astrophysical black hole systems, *Physics Reports*, 377, 389

[26] Ross R. R., Fabian A. C. (1993): The effects of photoionization on X-ray reflection spectra in active galactic nuclei, *MNRAS*, 261, 74

[27] Semerák O., Karas Vl., de Felice F. (1999): Parameters of Black Holes in Sources with Periodic Variability, *PASJ*, 51, 571

[28] Shapiro S., Teukolsky S. (1983): Black Holes, White Dwarfs and Neutron Stars. Cornell University, Ithaca, New York

[29] Shakura, N. I., Sunyaev, R. A. (1973): Black holes in binary systems, *A&A*, 24, 337

[30] Shapiro I.I. (1964): Fourth test of general relativity, *Phys.Rev.*, 13, 789

[31] Stella L. (1990): Measuring black hole mass through variable line profiles from accretion disks, *Nat*, 344, 747

[32] Stern B. E., Poutanen J., Svensson R., Sikora M., Begelman M. C. (1995): On the geometry of the X-ray emitting region in Seyfert galaxies, *A&A*, 449, L13

[33] Tanaka Y. et al. (1995), *Nat*, 375, 659

[34] Turner T. J. et al. (2002): Narrow Components within the Fe Kα Profile of NGC 3516: Evidence of the Importance of General Relativistic Effects?, *A&A*, 574, 123

[35] Turner T. J., Miller L., George I. M., Reeves J. N. (2006): Evidence for orbital motion of material close to the central black hole of Mrk 766, *A&A*, 445, 59

[36] Zeldovich B.Y. and Novikov I.D. (1971): Relativistic Astrophysics - Volume 1 Stars and Relativity. The University of Chicago Press, Chicago

[37] Zhang X.-H., Bao G. (1991): The rotation of accretion disks and the power spectra of X-ray 'flickering', *A&A*, 246, 21